Nucleic Acids Research, 2025, **53**, gkaf1199
https://doi.org/10.1093/nar/gkaf1199
RNA and RNA-protein complexes

A transcription termination mechanism for maintaining homogeneous protein expression

Sofia Esteban-Serna[1,2], Tove Widén[1,2], Mags Gwynne[1,2], Iseabail Farquhar[1,2], Michael R. Duchen[3], Peter S. Swain[1,2], Sander Granneman[1,2,*]

[1]Centre for Engineering Biology, University of Edinburgh, Edinburgh EH9 3BF, United Kingdom
[2]School of Biological Sciences, University of Edinburgh, Edinburgh EH9 3BF, United Kingdom
[3]Department of Physiology, University College London, London WC1E 6BT, United Kingdom

*To whom correspondence should be addressed. Email: Sander.Granneman@ed.ac.uk

Abstract

Premature transcription termination is a critical mechanism for repressing harmful, unproductive transcription. In *Saccharomyces cerevisiae*, premature termination by the Nrd1–Nab3–Sen1 (NNS) complex also triggers decay of mRNAs induced to counteract stress. However, why mRNAs might be upregulated and simultaneously targeted for degradation remains unclear. Our work reveals a novel role for NNS as a gene expression noise suppression system. Single-cell analyses demonstrate that targeted disruption of Nab3 binding to the highly conserved mitochondrial transporter *PIC2* not only alters its mRNA stability and protein levels but also dramatically increases cell-to-cell variability in Pic2 protein concentration. This specific perturbation in the regulation of a low-abundant transcript has substantial phenotypic consequences: significantly increased cell volumes, disrupted energy homeostasis, decreased growth rate, and altered expression of other NNS-regulated genes—all of which highlight the physiological importance of NNS control of Pic2 protein concentration. We show further that elevated levels of the human orthologue of Pic2, whose expression is tuned by the microRNA machinery, cause similar energy homeostasis defects, underscoring the evolutionary conservation of the tight regulation of the *PIC2* gene. Our results illustrate that targeted changes in the interaction of a single transcription termination factor (Nab3) with a specific RNA substrate can trigger significant system-wide defects and profoundly impact cellular fitness.

Graphical abstract

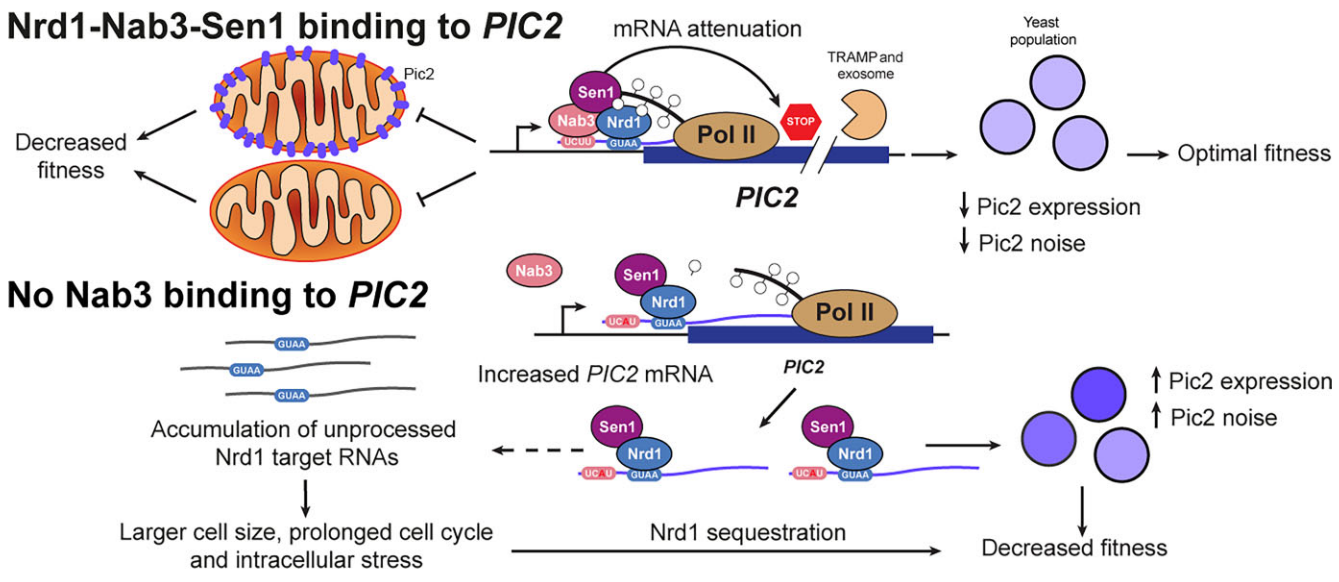

Introduction

Cells survive adverse conditions by rapidly reprogramming gene expression. At the beginning of a stress response, there is a genome-wide redistribution of both the transcription machinery and RNA-binding proteins (RBPs), particularly those involved in RNA decay [1]. Transcription termination plays critical roles in regulating adaptive responses in both prokaryotic and eukaryotic organisms. For example, in many

Received: February 4, 2025. **Revised:** October 8, 2025. **Accepted:** October 9, 2025

bacteria, the Rho RNA helicase plays critical roles in suppressing unproductive transcription and in conditional reprogramming of gene expression via premature transcription termination [2]. This allows for rapid adjustments in gene expression in response to environmental changes. In budding yeast, this role is attributed to the Nrd1–Nab3–Sen1 (NNS) complex, which mediates the maturation of small nuclear (snRNA) and small nucleolar RNAs (snoRNAs) as well as the degradation of cryptic unstable transcripts (CUTs) originating from pervasive bidirectional transcription [3–6]. Analogous to Rho, Sen1 plays a critical role in transcription termination by facilitating the release of the nascent transcript from RNA polymerase [7]. Moreover, Sen1 is conserved in higher eukaryotes (Senataxin) and is involved in unwinding harmful RNA–DNA duplexes [8]. Although not all NNS components are conserved in mammalian cells, complexes like integrator and restrictor exert a similar promoter–proximal transcriptional regulation by attenuating antisense transcription from the transcription start site of protein-coding genes [9].

Transcription termination by NNS starts with the Nrd1–Nab3 heterodimer binding a phosphorylated serine (Ser5P) residue in the C-terminal domain of RNA polymerase (Fig. 1A). Nrd1 and Nab3 subsequently recognize their cognate sequences in the RNA and recruit Sen1 to dismantle the polymerase elongation complex [3]. The NNS complex then recruits the Trf4–Air2–Mtr4 (TRAMP) complex to add short polyadenylation signals at the 3′ end of the released transcripts. These signals flag them for degradation by the exosome [3]. Since the NNS complex generally assembles during the synthesis of the first 100 ribonucleotides [10], the resulting transcripts are usually not longer than ∼500 nucleotides.

NNS also plays important roles in remodelling the transcriptome in response to nutrient availability [11, 12]. Surprisingly, under these conditions, messenger RNA (mRNA) transcripts from some induced protein-coding genes are simultaneously targeted by NNS for RNA decay [11, 12]. This implies that a fraction of the mRNAs produced during stress is immediately destroyed by the nuclear RNA decay machinery. However, the biological significance of this phenomenon remains unclear. Given the stochastic nature of Pol II transcription, we conjectured that transcribing stress-responsive genes and concurrently targeting their transcripts for premature termination by NNS may have evolved as a strategy to reduce overshooting of gene expression during nutrient scarcity. We speculate that this adjustment would be particularly relevant to genes encoding proteins which, when present at high levels, would pose a disadvantage to cells facing challenging environments.

To test these hypotheses, we focused on *PIC2,* an NNS target that is strongly upregulated during glucose starvation [12] and encodes a conserved mitochondrial phosphate and copper importer [13, 14]. Primarily, *PIC2* was selected as a model target because inadequate expression of its protein causes a clear growth defect against which we could benchmark our observations [14]. Furthermore, because Pic2 is functionally conserved in higher eukaryotes, we tested whether altered expression of *SLC25A3*, the mammalian homologue of Pic2, whose tight regulation is conserved but occurs via different mechanisms [15, 16], caused similar phenotypes to yeast.

We demonstrate that the NNS regulation of *PIC2* not only dampens protein expression but also ensures homogenous Pic2 protein concentrations across the population. Disrupting NNS regulation of *PIC2* had significant physiological consequences and affected the expression of multiple other NNS targets, suggesting that numerous genes are co-regulated through this mechanism. Incomplete binding of the NNS complex to *PIC2* resulted in decreased growth, defects in energy homeostasis, increased cell size, and delayed cell cycle progression. Our phenotypic and transcriptomic analyses suggest that the latter two defects are primarily due to impaired NNS termination at other targets.

Materials and methods

Yeast strain construction

All the strains engineered in this study are derived from the BY4741 reference [17].

Homologous recombination

Polymerase chain reaction (PCR)-based modification was employed to fuse *GFP* downstream *PIC2*, to integrate HIS6-TEV-3xFLAG (HTF) epitopes distally to *NAB3*, *NRD1*, *RPO21*, and *SEN1*; and to delete *PIC2* in the *pic2Δ0::HIS3* and the *pic2Δ::KANMX6* mutants according to widely used protocols [18, 19]. The coding sequence of *GFP*, the His6-TEV-3xFLAG (HTF) tag and the *HIS3* cassette were amplified from the pFA6a-GFP(S65T)-His3MX6 [18], pBS1539::HIS6-TEV-3xFLAG URA3 [20], pFA6a His3MX6 [18], and pFA6a-kanMX6 [21] vectors using the oligonucleotides listed in Supplementary Tables S1–3, respectively.

CRISPR–Cas9

A previously described CRISPR–Cas9 gene editing approach [22] was applied to induce mutations in the promoter region of *PIC2*. The primers used are listed in Supplementary Table S4.

Plasmid construction

The pTEF1-yEGFPCLN2PEST-pRS406 [23] backbone was cleaved by EcoRI/AscI to allow the integration of fragments containing the sequence of *PIC2*, which were amplified by primers containing MfeI and AscI restriction sites (Supplementary Table S5). The recombinant plasmid-encoded *URA3* as an auxotrophic marker and was transformed into the BY4741 strain to yield the *pTEF1-PIC2* mutant. To ensure medium uniformity across samples and experiments, all other strains used in this study were transformed with the unaltered pRS406 plasmid [24], which also codes for the same selectable marker.

To perform cross-linking and analysis of cDNA (CRAC) experiments on *Pic2–GFP* strains overexpressing *PIC2*, we transformed the strains in which Nab3 and Nrd1 were chromosomally tagged to HTF (see homologous recombination) with a version of the *pTEF1-PIC2* plasmid in which the *URA3* cassette was replaced with a *LEU2* marker (amplified with the oligonucleotides outlined in Supplementary Table S5). This enabled the selection of *PIC2*-overexpressing clones in strains where the *URA3* cassette had already been integrated alongside the HTF epitope. The parental *Pic2–GFP* reference, as well as the *pic2Δ::KANMX6* deletion strain generated in this background, were transformed with the pRS415 *LEU2*-encoding plasmid.

To generate the pcDNA5/FRT *SLC25A3-HTF* plasmid, *SLC25A3* was fused to an HTF tag, and NotI and XhoI restriction sites were included immediately upstream and

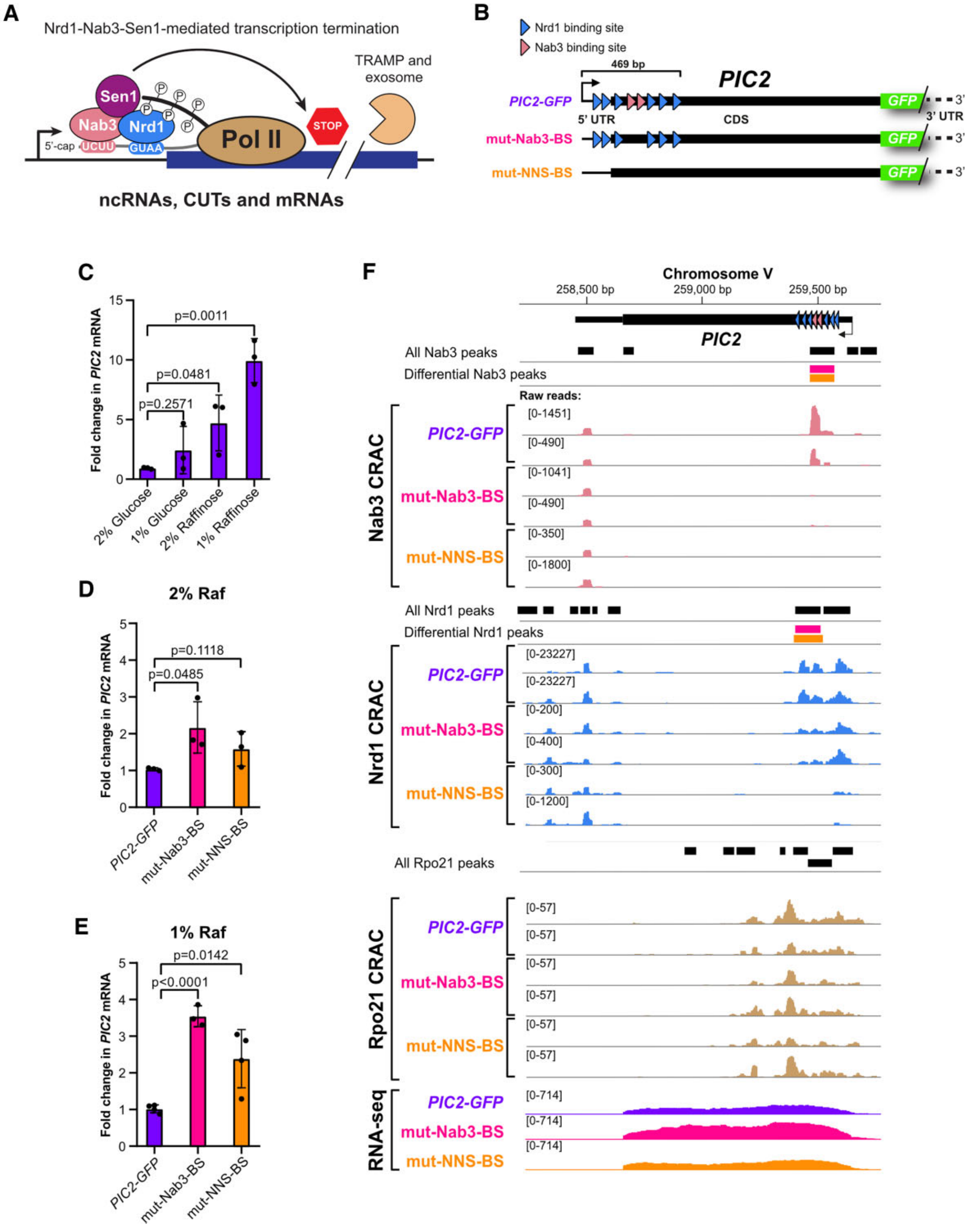

Figure 1. Mutating NNS-binding sites in *PIC2* increases its expression. (**A**) Schematic representation of NNS-mediated termination. Nrd1, Nab3, and Sen1 are co-transcriptionally recruited to RNA Pol II through an interaction with phosphorylated serine-5 in the CTD of Pol II. The binding of Nab3 and Nrd1 to specific sequences in the RNA transcript pauses Pol II and activates Sen1, which then terminates transcription. The truncated nascent transcript is targeted for degradation by the TRAMP–exosome complex. (**B**) Diagrammatic summary of the Nab3 and Nrd1 RNA binding sites in *PIC2* and our two modified strains: mut-Nab3-BS and mut-NNS-BS. (**C**) Fold changes of *PIC2* mRNA levels in the *Pic2–GFP* strain relative to 2% glucose. Bar plots display means and SDs of three independent biological repeats. *P*-values were calculated using a two-sided unpaired Student's *t*-test. (**D** and **E**) Fold changes of *PIC2* mRNA levels in the mut-Nab3-BS and mut-NNS-BS mutants compared to the parental strain in two different raffinose concentrations (2% and 1%). Bar plots display means and SDs of three independent biological repeats. *P*-values were calculated using a two-sided unpaired Student's *t*-test. **(F)** Removing Nab3-binding sites in *PIC2* does not completely prevent Nrd1 binding. Snapshots of read distributions obtained in Nab3 CRAC (top panel), Nrd1 CRAC (second panel), Rpo21 (Pol II) CRAC (third panel), and RNA-seq data (last panel) of the parental *Pic2–GFP* strain and mut-Nab3-BS and mut-NNS-BS mutants. CRAC datasets show results from two independent repeats. To compensate for differences in library coverage, the raw reads shown on the *y*-axes were adjusted to display similar signals in neighbouring peaks that had not been deemed DB by the DBPeaks package. Rpo21 CRAC tracks, as well as the RNA-seq signal coverage, are provided in reads per million (RPM). The RNA-seq data track was generated by merging biological triplicate datasets. Nrd1- and Nab3-binding sites were identified using pyCalculateFDRs from the pyCRAC package [34]. Differential binding sites identified by DBPeaks in mut-Nab3-BS (pink) and mut-NNS-BS (orange) are indicated.

downstream of the desired construct to enable digestion and subsequent integration of the *SLC25A3-HTF* coding sequence between the CMV promoter and the BGH polyadenylation signal encoded in the pcDNA5/FRT TO vector. The codon sequence of the *SLC25A3-HTF* construct was optimized for *Homo sapiens* by GeneArt (Thermo Fisher Scientific) and inserted into a standard (pMX) vector encoding a kanamycin-resistance selection marker. The designed vector was supplied as part of the GeneSyn service provided by GeneArt (Thermo Fisher Scientific).

Mammalian cell line generation

Flp-In™ T-REx™ HEK 293 cells were co-transfected with three different vectors: one encoding SLC25A3 with its accompanying FRT recombination site, pcDNA5/FRT SLC25A3-HTF; another one coding for the flipase recombinase, pOG44; and a third one containing the tetracycline repressor and a blasticidin-resistance gene for selection, pcDNA6/TR.

Flp-In™ T-REx™ HEK 293 transfection

Having depleted antibiotics from the medium 1 h before transfection, we dissolved 5 μg of each plasmid in OptiMEM medium (Thermo Fisher Scientific) to a final volume of 1250 μl. Similarly, for each 15-cm sample dish to be transfected, 15 μl of lipofectamine 2000 (Thermo Fisher Scientific) was mixed with 1235 μl of OptiMEM. Both mixtures were then combined, mixed by pipetting and incubated at room temperature for at least 20 min to allow the formation of DNA–lipofectamine complexes that can penetrate the mammalian plasma membrane of the cells in a single plate. Cells were then kept at 37°C for 1 h before exposing them to a final concentration of 15 μg/ml blasticidin and 100 μg/ml hygromycin within their growth medium.

Yeast growth conditions

Yeast cells were grown in synthetic complete (SC) medium containing or lacking uracil (SC -Ura) or leucine (SC -Leu). Yeast strains encoding an auxotrophic marker were selected by growth in SC medium lacking uracil or L-histidine. Throughout microplate reader fluorescence assays, yeast cells were grown in SC medium lacking folic acid and riboflavin (LoFlo) to minimize background fluorescence. While a concentration of 2% (w/v) of a given sugar was considered rich medium, a 1% (w/v) concentration posed a nutritional deprivation challenge to which cells in culture must adapt. Since fermentable carbon sources such as glucose are known to downregulate respiration, raffinose was used to formulate the media used in all experiments of this study. Given that the expression of some hexose transporters can be influenced by previous exposure to fermentable sugars such as glucose [13, 14], all strains were pre-cultured in medium containing 2% (w/v) pyruvate for 48 h prior to the start of the experiment [25]. This pre-growth stage ensured that the expression profiles of the different strains had a homogeneous starting point.

All liquid cultures were incubated at 30°C with shaking at 190 rpm. To facilitate growth in plates, medium for these was prepared using 2% (w/v) glucose as a carbon source and solidified upon the addition of agar to a final concentration of 1% (w/v). Cells grown in Petri dishes were incubated at 30°C in a static incubator for 48 h and kept at 4°C afterwards. Yeast peptone dextrose adenine (YPDA)-rich medium was used for growing cells before transformation and freezing. For the selection of transformants during the CRISPR–Cas9 genetic modification procedure, cells were plated in YPDA medium supplemented with 1% (w/v) agar and nourseothricin (100 μg/ml). The cells used in all experiments were harvested at OD_{600} 0.5 except those used in CRAC, which were gathered at OD_{600} 1. For microscopy and polarographic quantification of oxygen consumption, cells were grown in 5 ml cultures. Cytometry experiments, as well as RNA and protein extractions, were performed on cells collected from 25 ml cultures. Nab3 depletion in the *NAB3-FRB* strain was achieved by supplementing the pertinent 25 ml cultures with 1 μg/ml of rapamycin (Sigma–Aldrich). Transcription inhibition for RNA decay measurements was conducted by treating 100 ml cultures with thiolutin (Abcam) at a final concentration of 3 μg/ml. CRAC samples for *Pic2–GFP*, mut-Nab3-BS, and mut-NNS-BS were obtained from 500 ml (for Nab3 and Nrd1 libraries) or 1 L (for Sen1) SC -Ura cultures containing 1% (w/v) raffinose. CRAC experiments comparing Nab3 and Nrd1 occupancy in the *pTEF1-PIC2* and *Δpic2* mutants with the *Pic2–GFP* reference were conducted on 500 ml cultures grown in SC -Leu. RNA and protein extractions, as well as CRAC experiments, were performed on cells that were either pelleted by centrifugation (3202 rcf, 5 min) or filtered after cross-linking, snap-frozen by submersion in liquid nitrogen, and stored at −80°C.

Flp-In™ HEK 293 cell growth conditions

Cells were grown in the Dulbecco's Modified Eagle Medium (DMEM) containing 10% (v/v) foetal bovine serum (FBS), 2 mM L-glutamine, potassium penicillin (100 units/ml), and streptomycin sulphate (100 μg/m,). While the unmodified parental Flp-In™ HEK 293 cell line was grown in the presence of Zeocin™ (15 μg/ml), blasticidin (15 μg/ml) and hygromycin B (100 μg/ml) were supplemented to the growth medium of transfected cells. Transfected Flp-In™ HEK 293 cells were grown in six-well plates to a confluence of ∼80%–90% before the start of all phenotypic characterization experiments, and overexpression of the inserted *SLC25A3-HTF* was induced by adding 0.2 μg/ml of doxycycline to the growth medium 24 h prior to the start of the experiment. To determine the minimum concentration of doxycycline required for significant overexpression of SLC25A3-HTF, its abundance was estimated by western blot at a range of doxycycline concentrations recommended by the cell line manufacturer.

Measuring growth and oxidative stress tolerance in yeast and mammalian cells

Yeast cells from a culture in the mid-logarithmic growth phase were resuspended in fresh medium to a starting OD_{600} of 0.1. Two hundred microlitres were transferred to three separate wells of a UV-sterilized 96-well black non-treated polystyrene microplate (Thermo Fisher Scientific) and its accompanying lid (Grenier). Triplicate controls comprising the same volume of sterile medium were also included for each examined condition. Absorbance and fluorescence were monitored in Infinite F200 (Tecan) microplate readers.

For Flp-In™ HEK 293 cells, 0.5 mM of hydrogen peroxide or an equivalent volume of sterile water were added to tested and control populations, respectively. Trypan blue (Thermo Fisher Scientific) was used to measure the viability of cell populations immediately after exposure to hydrogen peroxide or water and 18 h after their addition. Counting was performed in a Countess 3 automated cell counter (Thermo Fisher Scientific). Two technical measurements were performed for each of the three biological assays that were completed per cell line and condition.

RNA immunoprecipitation

Cells were defrosted on ice and resuspended in 250 µl of lysis buffer. One millilitre of 0.5 mm zirconia beads (Thistle Scientific) was added, and samples were vortexed vigorously for five 1-min intervals followed by four 1-min incubations on ice. After pipetting another 750 µl of lysis buffer into each tube, samples were vortexed and centrifuged at 4°C (3202 rcf, 15 min) to remove cell debris. Fifty microlitres of cell lysates was extracted as input (whole transcriptome) references and stored at −80°C. The remaining extracts were spun down in an additional centrifugation step (10 621 rcf, 20 min) at 4°C. The remaining volume (∼900 µl) underwent a 2-h incubation with 30 µl of anti-FLAG® M2 magnetic beads (Sigma–Aldrich, M8823-5ML), which had been previously washed two times with 1 ml of lysis buffer. Afterwards, beads were washed four times with 1 ml of ice-cold lysis buffer and nutated during 5 min at 4°C in between each wash. The beads were then mixed with 100 µl, and Sen1 was eluted by adding 600 µl of GTC phenol. RNA was isolated from the resulting fractions and compared to the input samples using reverse transcription coupled to quantitative PCR (RT-qPCR).

RNA decay measurements

RNA stability assays were performed as described [26]. Briefly, triplicate 100 ml cultures of SC -Ura containing 1% (w/v) raffinose were grown to an OD_{600} of 0.5. Once they reached the desired growth stage, 5 ml of culture were spun down (3202 rcf, 5 min) and snap frozen. Cells were then incubated with 3 µg/ml of thiolutin (Abcam) to block RNA polymerase II (Pol II) transcription. Five millilitres of culture was harvested from the treated flasks every 5 min for up to 30 min following thiolutin addition.

RNA extractions

Cells were thawed on ice and denatured by the addition of 200 µl of guanidinium thiocyanate (GTC) acid phenol mix. While mammalian cell lysis was achieved by vortexing at maximum speed twice for 30 s and incubation in a thermoblock for 5 min at 30°C with shaking at 300 rpm, yeast cell lysis was performed by adding 400 µl of glass beads to each sample and vortexing all tubes at full speed for five 1-min intervals separated by four 1-min incubations on ice. An additional 1.5 ml of GTC phenol mix was then added to the latter samples. Yeast samples were incubated at 65°C for 10 min before being placed on ice for another 10 min. Eight hundred microlitres and hundred microlitres of sodium acetate mix (3.3 ml of 3 M NaOAc, pH 5.2, 0.2 ml of 0.5 M EDTA, pH 8, 1 ml of 1 M Tris–HCl, pH 8, water to 100 ml) and 1.5 ml and 200 µl of chloroform were pipetted into yeast and mammalian extracts, respectively, before vortexing each lysate at maximum speed for 5 s. Samples were centrifuged at 4°C (10 621 rcf, 30 min), and the resulting aqueous phase was transferred into a new tube containing an equivalent volume of phenol:chloroform:isoamyl alcohol mix. The mixtures were vortexed vigorously and centrifuged at 10 621 rcf for 5 minu. Once more, the aqueous phase of each sample was mixed with an equal volume of chloroform:isoamyl alcohol and vortexed at maximum speed before centrifugation at 10 621 rcf for 5 min. Finally, the aqueous phase of each sample was relocated to tubes containing three volumes of 96% ethanol. The mix was vortexed vigorously and preserved at −80°C for at least 30 min or at −20°C overnight. Following ethanol precipitation, samples were spun at 10 621 rcf for 30 min at 4°C. After discarding the resulting supernatants, 70% ethanol was pipetted into each tube. After centrifuging samples at 10 621 rcf for 5 min at 4°C, ethanol was removed, and pellets were left to air-dry for ∼5 min before resuspension in DEPC water. Finally, RNA concentrations were measured in the Qubit™ 4 fluorometer (Thermo Fisher Scientific) using the Qubit™ RNA HS assay kit (Thermo Fisher Scientific).

Real-time quantitative reverse transcription PCR

RNA extracts were purified by DNase treatment with RQ1 RNase-Free DNase (Promega) and reverse-transcribed using SuperScript™ IV reverse transcriptase and random primer mix (New England Biolabs). Samples were mixed with Briliant III ultra-fast SYBR® green qPCR master mix (Agilent Technologies) and amplified within a 384-well plate (Roche) in LightCycler® 480 qPCR device (Roche). Three reference genes were inspected in every assay: while we used *ACT1*, *ALG9*, and *PGK1* for yeast samples, we monitored *ACTB*, *GAPDH*, and *RPL39* in mammalian ones. For the Sen1 RNA-immunoprecipitation experiments, we used *ALG9*, *NEL025c*, and *snRN13* as reference genes. Sequences for all RT-qPCR primers are outlined in Supplementary Table S6.

Cross-linking and analysis of cDNAs

When SC -Ura cultures containing 1% (w/v) raffinose reached an OD_{600} of 1, cells were UV cross-linked (254 nm; 500 mJ/cm^2) in the Vari-X-linker (UVO_3; [12, 27]) and rapidly filtered on 0.8 µm membranes (Merck) using a filtration device connected to a vacuum pump [12, 27]. Membranes were collected in 50 ml tubes, flash-frozen by submersion into liquid nitrogen, and stored at −80°C until the day of the experiment.

On the day of the experiment, pellets were resuspended in a volume of lysis buffer [150 mM NaCl, 50 mM Tris, pH 7.8, 0.1% (v/v) Nonidet *P*-40, 1 EDTA-free protease inhibitor cocktail (Roche) per 50 ml, and 5 mM β-mercaptoethanol] corresponding to twice their mass. Lysates were then transferred to fresh 50 ml tubes, where they were mixed with two volumes of 0.5 mm zirconia beads (Thistle Scientific) and vortexed at maximum speed for five 1-min intervals alternated with 1-min incubations on ice. An additional volume of lysis buffer was pipetted into each sample before partitioning the cell debris by centrifugation at 4°C (3202 rcf, 15 min) and spinning down lighter impurities in an additional centrifugation step (10 621 rcf, 20 min) at 4°C. Immunoprecipitation of the labelled protein from the supernatant was achieved during a 2-h incubation of the sample with 75 µl of anti-FLAG® M2 magnetic beads (Sigma–Aldrich, M8823-5ML), which had been previously washed three times with 1 ml of TN150 buffer. Immobilized beads underwent three 5-min washes with TN1000 buffer [50 mM Tris, pH 7.8, 1 M NaCl, 0.1% (v/v) Nonidet *P*-40, and 5 mM β-mercaptoethanol] and three additional 5-min washes in 2 ml of TN150 buffer [150 mM NaCl, 50 mM Tris, pH 7.8, 0.1% (v/v) Nonidet *P*-40, and 5 mM β-mercaptoethanol]. Afterwards, beads were resuspended in 550 μl of TN150 and incubated with 1 μl of a 1:100 dilution of RNace-It™ for exactly 5 min at 37°C. To prevent overdigestion of co-immunoprecipitated transcripts and elute the bait proteins from the anti-FLAG beads, the solution was mixed with 0.4 g of guanidium hydrochloride (Gu-HCl) and the necessary volume of NaCl and imidazole (pH 8.0) to reach a final concentration of 300 and 10 mM, respectively. After removing the beads, samples were pipetted onto 50 μl of Ni-NTA agarose resin (Qiagen) equilibrated with wash buffer I [6 M Gu-HCl, 10 mM imidazole, 300 mM NaCl, 50 mM Tris–HCl, pH 7.8, 0.1% (v/v) Nonidet *P*-40, and 5 mM β-mercaptoethanol] and incubated at 4°C overnight while rotating at 12 rpm.

Upon Ni-NTA binding, beads were transferred to Pierce columns (Thermo Fisher Scientific) and washed twice with 500 μl of wash buffer I before undergoing three additional washes of 500 μl with NP-PNK buffer [10 mM $MgCl_2$, 50 mM Tris–HCl pH 7.8, 0.1% (v/v) Nonidet *P*-40, and 5 mM β-mercaptoethanol]. Alkaline phosphatase treatment was performed by resuspending immunoprecipitated RNA–protein conjugates in 80 μl of NP-PNK buffer containing 4 units of FastAP thermosensitive alkaline phosphatase (Thermo Fisher Scientific) and 80 units of RNasin® ribonuclease inhibitor (Promega) and incubating the samples at 37°C for 1 h in the case of Nab3 and Nrd1, or 15 min for Sen1. Dephosphorylation was stopped upon the addition of 500 μl of wash buffer. Having equilibrated the Ni-NTA agarose with three washes of 500 μl with NP-PNK, we performed adapter ligation by resuspending the beads 80 μl of reaction mix containing 0.6 μM of the applicable App-PE 3′ adapter (Supplementary Table S7), 30 units of T4 RNA ligase 2 truncated K227Q (New England Biolabs), 60 units RNasin® (Promega), and 10% (w/v) polyethylene glycol 8000 (PEG 8000). The reaction took place at 25°C for 6 h for Nab3 and Nrd1 CRAC and for 3 h during Sen1 CRAC.

After washing once with 500 μl of wash buffer I and three times with 500 μl of NP-PNK buffer, we 5′ end radiolabelled co-immunoprecipitated RNAs by incubating the Ni-NTA resin with 60 μl of NP-PNK buffer containing 30 μCi ^{32}P-γATP (PerkinElmer) and 30 units of T4 polynucleotide kinase (New England Biolabs). After a 40-min incubation of the reaction at 37°C, ATP (Roche) was supplemented to a final concentration of 1 mM, and the reaction continued for another 20 min. The reaction was stopped by washing three times with 500 μl of wash buffer I and three 500 μl washes of NP-PNK buffer followed before the addition of the 5′ linker ligation mix. The reaction took place in a volume of 80 μl of NP-PNK buffer supplemented with 1.25 μM of the fitting adapter, 40 units of T4 RNA ligase 1 (New England Biolabs), 80 units of RNasin®, and 10 mM ATP (Roche). 5′ adapter ligation was left to proceed overnight at 16°C for all bait proteins. The remaining steps of the protocol were executed as in previous reports [12, 28]. After pooling suitable libraries together, all Nab3, Nrd1, Sen1, and Rpo21 samples for *Pic2–GFP*, mut-Nab3-BS, and mut-NNS-BS, and their corresponding traces were submitted to Novogene, where paired-end sequencing of 150 bp-reads was performed in a NovaSeq 6000 system (Illumina). The Nab3 libraries acquired from *Pic2–GFP*, *pTEF1-PIC2*, and *pic2Δ* were prepared using a MiniSeq high-output 75-cycle reagent cartridge (Illumina) and sequenced in a benchtop MiniSeq System (Illumina).

Western blotting

Yeast and Flp-In™ HEK 293 cell lysates were prepared by addition of two volumes of lysis buffer [50 mM Tris–HCl, pH 7.8, 150 mM NaCl, 0.1% (v/v) Nonidet *P*-40, 1 cOmplete™, EDTA-free Protease Inhibitor Cocktail (Roche) per 50 ml, and 5 mM β-mercaptoethanol) to 1 g of cell pellet. Whereas no mechanical force was required for mammalian cell homogenization, yeast samples were combined with 0.5 mm zirconia beads (Thistle Scientific) before being vortexed at full speed for five 1-min intervals followed by four 1-min incubations on ice. Cell debris was removed by centrifugation at 10 621 rcf for 20 min. The protein concentration of each supernatant was measured using the Qubit™ 4 fluorometer (Thermo Fisher Scientific) and normalized to that of the most diluted sample. Protein analysis occurred in NuPAGE™ (Thermo Fisher Scientific) precast polyacrylamide gels. Whilst lysates assigned to Nab3-HTF, Nrd1-HTF, and SLC25A3-HTF detection were separated in 4%–12% gradient Bis–Tris gels with MOPS running buffer (Thermo Fisher Scientific), samples designated to the inspection Sen1-HTF were partitioned in 3%–8% gradient Tris-acetate gels with Tris-acetate running buffer (Thermo Fisher Scientific). All electrophoreses ran for 1.5 h at 120 V. Proteins were transferred onto 0.2 μm nitrocellulose membrane and immunoblotting was performed using a 1:5000 dilution of a monoclonal anti-FLAG® M2-Peroxidase (HRP) antibody (Sigma–Aldrich, A8592; for HTF-fused proteins), a 1:1000 dilution of anti-GAPDH recombinant rabbit monoclonal antibody (Thermo Fisher Scientific, RM114; for the loading control in mammalian cell samples, GAPDH) and a 1:5000 dilution of an anti-RNA Pol II antibody, clone CTD4H8 (Sigma–Aldrich, 05-623-25UG; for the loading control of yeast samples, Rpo21). Incubation with primary antibodies occurred overnight at 4°C. While the anti-FLAG antibody was directly imaged after chemiluminescence with the Pierce™ enhanced chemiluminescence (ECL) kit (Thermo Fisher Scientific), the anti-Rpo21 and anti-GAPDH antibodies underwent a 2-h hybridization to 1:5000 dilutions of anti-mouse IRDye 800CW (LI-COR Biosciences) and goat anti-rabbit IRDye® 680RD (LI-COR Biosciences) secondary ones at room temperature. HTF-tagged proteins were visualized by applying the automatic chemiluminescence exposure settings in the Amersham ImageQuant™ 800 system (Cytvia Life Sciences). Membranes requiring fluorescence imaging were exposed to the IR long (775 nm) and IR short (660 nm) channels of the same device for 15 s and 5 min, respectively.

Flow cytometry

DNA quantification for cell cycle analysis

Five millitres of cells from mid-exponential-phase cultures were pelleted and immediately fixed by the addition of an equal volume of ice-cold 70% ethanol and an overnight incubation at −20°C. On the next day, cells were permeabilized with 800 μl of 50 mM sodium citrate buffer (pH 7.2) and a 10-min incubation at room temperature. This step was repeated once more before adding RNace-It™ ribonuclease cocktail (i.e. a mixture of RNase A and RNase T1; Agilent Technologies) to a final concentration of 0.1 mg/ml (i.e. 15 μl of 2 mg/ml stock) and incubating the samples overnight at 37°C. Following RNA degradation, proteins were digested upon the addition of 10 μl of 20 mg/ml proteinase K (Roche) and subsequent incubation at 55°C for 2 h. Afterwards, cell aggregates were disrupted by sonication (5 s, 25 μm). At this stage, samples could be stored for up to 1 month at 4°C or stained with 50 μg/ml propidium iodide (Sigma–Aldrich) for flow cytometry. In the latter case, 200 μl of each resulting sample were pipetted into individual wells of a clear 96-well plate (Thermo Fisher Scientific) for inspection in a BD LSR-Fortessa (BD Biosciences) at the Flow Cytometry Facility for the School of Biological Sciences of the University of Edinburgh. A total of 10 000 events were recorded per acquisition.

Fitness assay

A volume holding an equivalent to OD_{600} 0.0005 of the tested strain was transferred into 5 ml of fresh medium before adding the red fluorescent strain (Ura7-mCherry) at a final identical OD_{600}. Cells were then left to compete in the medium overnight. After 18 h, 1 ml of culture was pelleted (3202 rcf, 5 min) and resuspended in phosphate-buffered saline (PBS) prior to inspection in a BD LSR-Fortessa (BD Biosciences). A minimum of 20 000 events were recorded per competition culture. A volume corresponding to OD_{600} 0.0005 of the mid-logarithmic-phase culture was transferred to 5 ml of the same sterile medium to continue monitoring the competition throughout time. Subsequent samples were gathered at 36- and 60-h post-inoculation for analogous flow cytometry acquisitions.

Mating assay

Pic2–GFP, mut-Nab3-BS, and mut-NNS-BS (MATa) were mixed with a BY4742 (MATta) in YPDA plates and incubated at 30°C. The following day, single colonies were re-streaked into fresh YPDA plates and stored at 30°C to allow growth overnight. Mating tester plates were then prepared to screen for diploids, which were able to grow independently from the mating factor (a or a) which had been used to coat such plates. Potential diploids underwent sporulation upon re-streaking in SPO sporulation medium [0.3% (w/v) potassium acetate, pH 7]. Throughout an incubation at 30°C for up to 3 days, plates were checked regularly for tetrads, and once they were identified, these were collected for digestion. To this end, cell samples were resuspended in 20 μl of digestion solution [1 mg/ml of zymolase (AMS Biotechnology) dissolved in 1 M sorbitol] and subsequently incubated at room temperature for 8 min. To stop the reaction, 1 ml of sterile water was added to each sample. Twenty microlitres of the resulting solution were pipetted on the border of a fresh YPDA plate and left to slide through its diameter before being air-dried. Once all the volume of the digestion solution had evaporated, a minimum of 8 tetrads were dissected onto each half of the plate. Dissection plates were then incubated at 30°C overnight before proceeding with a mating-type check of the sister spores within each tetrad by colony PCR or microscopy inspection. Dissections yielding an a to α ratio of 2:2 were deemed successful, and hence, we proceeded to quantify the cell size of their constituent spores.

Quantification of mitochondrial membrane potential with confocal microscopy

Mitochondrial membrane potential was assessed using tetramethyl rhodamine, methyl ester (TMRM; Sigma–Aldrich), a cell-permeable, positively charged, red fluorescent dye that accumulates in mitochondria proportionally to their activity. TMRM was added to mid-exponential cultures at a final concentration of 50 nM. After a 30°C with shaking at 190 rpm, 100 μl of cell solution were then pipetted into the wells of a black cytll plate with bottom glass (Grenier), which had been pre-coated with 0.1% (w/v) poly-L-lysine (Sigma–Aldrich). Poly-L-lysine effectively allowed temporary immobilization of some cells during live imaging.

Adherent Flp-In™ HEK 293 cells were grown directly in a 96-well plate with a bottom glass. Over 12 000 mammalian cells were seeded 4 days before the imaging was performed. Fresh DMEM and the relevant antibiotics were provided every 48 h. Two days after seeding, fresh medium was replenished, and *SLC25A3* overexpression was induced with 0.2 μg/ml doxycycline 24 h before the start of the experiment. On the day of the experiment, DMEM was removed, and cells were washed twice with 100 μl of PBS and finally incubated at 37°C in recording medium [phenol red-free DMEM (Thermo Fisher Scientific) supplemented with 10 mM glucose, 1 mM glutamine, and 10 mM HEPES, pH 7.4]. Thirty minutes before imaging a given well, 25 nM of TMRM was added to the recording medium. To prevent membrane transporters from extruding the dye, cells were also treated with 25 μM of verapamil (Sigma–Aldrich), an efflux pump inhibitor.

Imaging was then performed in an LSM 880 microscope (Zeiss) at the Medical Sciences Building Confocal Imaging Facility at University College London. While imaged, yeast and mammalian samples were kept at 30°C or 37°C, respectively, inside an incubation chamber (Zeiss). For yeast acquisitions, TMRM was excited with a 561 nm argon laser with an output power of 0.2 mW, the pinhole was set at 2.67 arbitrary units (a.u.), and the detector gain was fixed at 850. Whereas red fluorescence parameters remained unaltered for all acquisitions, the detector gain for the T-PMT channel had to be adjusted to successfully view the outline of the cells in each sample. In both channels, 10 z-stacks were taken for TMRM images, with a spacing of 0.6 μM between slices. For Flp-In™ HEK 293 imaging, TMRM settings were slightly modified compared to those of yeast cells: the argon laser power was decreased to 0.1 mW to minimize radiation-induced stress in the cells, the pinhole was reduced to 1.62 a.u. to increase the resolution of the stained areas and, owing to the larger volume of human cells, the *z*-stacking parameters were changed to acquire 14 regularly spaced slices spanning 13 μm. To verify that the signal captured in the red fluorescence channel emerged solely from TMRM, we acquired control images of unstained yeast cells. Additionally, to confirm that TMRM was exclusively being sequestered by active mitochondria, we re-imaged stained samples in which mitochondrial membrane potential was collapsed upon the addition of carbonyl cyanide-p-trifluoromethoxy phenylhydrazone (FCCP; Sigma–Aldrich), a powerful uncoupler of oxidative phosphorylation.

Polarographic quantification of oxygen consumption rates

Oxygen consumption rates were measured using a high-resolution O2K respirometer (Oroboros). Cells from mid-exponential cultures were resuspended into fresh sterile medium to reach a final OD_{600} of 0.1. Two millilitres of these cell solutions were injected into a pre-warmed chamber before recording basal respiration measurements at 30°C or 37°C for yeast or HEK293, respectively.

NADH fluorescence measurements

Fluorescence measurements were recorded using the OD_{600} absorbance and NADH fluorescence modes of the CLARIOstar Plus (BMG LABTECH) microplate reader. OD_{600} measurements were obtained to enable the normalization of the NADH fluorescence values to cell numbers. Given that the nicotinamide moiety of NADPH would also fluorescence in this mode, the raw recording is, in principle, also dependent on the status of the NADP(H) pool. However, the concentration of NAD(H) is ~100 times larger than that of NADP(H) [29], and the NADP pool is stably maintained in its reduced state (i.e. at least 20:1 NADPH to NADP) [30]. Therefore, even the raw measured fluorescence signal is broadly reflective of the state of the NAD(H) pool.

To compensate for the effect that emissions proceeding from NADPH may have in the NADH measurement, the resting fluorescence value was normalized to the fluorescence recordings in samples in which the NADH/NAD^+ ratio reached its minimum and maximum, respectively [31]. While the basal measurement was taken in untreated cells, another set of cells was exposed to FCCP, which elicits maximal respiration and, consequently, drives full oxidation of the NAD pool to its NAD^+ state. Thus, any NADH signal recorded upon the addition of FCCP was assumed to correspond to a background measurement for the NADH autofluorescence acquisitions. Conversely, another set of samples was treated with sodium cyanide (NaCN; VWR International), which blocks complex IV of the electron transport chain and impedes respiration. Even though NaCN-mediated inhibition of complex IV is not substrate-dependent, the physiological response of the cell to a shutdown of the electron transport chain is to increase the production of substrates that can be fed to the ETC to resume respiration. Consequently, the cell fully reduces its NAD pool, thereby yielding its maximum NADH fluorescence. NADH fluorescence values were recorded 2 min after the addition of the drugs. Due to their different susceptibility to FCCP and NaCN, yeast cells were exposed to 15 μM and 1.25 mM of these drugs, respectively, whereas Flp-In™ HEK 293 cells were treated with 1 μM of FCCP and 1 mM NaCN. Whereas yeast acquisitions were performed at 30°C, HEK 293 ones occurred at 37°C.

RNA sequencing

RNA extracts were treated with RQ1 RNase-Free DNase as per the manufacturer's guidelines. The quality of the RNA samples was then using an Agilent 2100 bioanalyzer (Agilent Technologies) with RNA 6000 pico chip (Agilent Technologies) according to the manufacturer's instructions. Samples with an RNA integrity number (RIN) score >7 were submitted to Novogene for paired-end sequencing of 150 bp-reads in a NovaSeq 6000 system (Illumina). Before sequencing, samples underwent a rRNA depletion step, and libraries were generated using the TruSeq preparation protocol (Illumina).

Sample preparation for proteome profiling

Cell pellets were thawed and resuspended in 20 μl of 4% (w/v) SDS dissolved in 100 mM Tris–HCl pH 8 and incubated at 95°C for 30 min. Samples underwent three sonication cycles (10 seconds "on", 5 seconds "off") at an amplitude of 5 μm. Tris–HCl pH 8 was added to dilute SDS concentration to 1% (w/v). Additionally, dithiothreitol (DTT) was supplemented to a final concentration of 10 mM before incubating the lysates at 50°C for 30 min. Samples were then centrifuged at 20 817 rcf for 15 min before measuring the protein concentration in the resulting supernatant. A volume holding 100 μg was aliquoted for each sample before adding urea to a final concentration of 6 M. Following mixing, denatured proteins were cleaned with filter-aided sample preparation columns (FASP, Microcon-30kDa centrifugal filter unit, Millipore, MRCF0R030). After centrifugation (14 000 *g*, 40 min), the flow-through fraction was discarded, and the filter membrane was further washed with 200 μl of 8 M urea in 100 mM Tris–HCl, pH 8. The proteins in the filter were then alkylated with 100 μl of 5 mM iodoacetamide (IAA, Sigma–Aldrich) dissolved in 8 M urea. Alkylation occurred at room temperature in the dark for 20 min. The filter membrane was then washed once with 100 μl of 8 M urea Tris–HCl, pH 8, and twice with 100 μl of 50 mM ammonium bicarbonate (ABC, Sigma–Aldrich). Upon centrifugation (14 000 *g*, 10 min) and subsequent removal of the flow-through fraction, 1 μg of mass spectrometry (MS/MS) grade trypsin protease (Thermo Fisher Scientific) was diluted into 39 μl ABC and applied to the column of each membrane. All samples were incubated at 37°C overnight until an additional 40 μl of ABC were added to each sample, and its peptides were collected by centrifugation (14 000 *g*, 10 min). The peptide concentration was measured using a Qubit™ 4 fluorometer (Thermo Fisher Scientific) before samples were acidified to pH ≤ 3 with the pertinent volume of 10% (v/v) trifluoroacetic acid (TFA) and desalted in C18 extraction filters (Thermo Fisher Scientific) contained within 200 μl microtips. Membranes were activated upon passing (14 000 *g*, 10 min) of 15 μl of methanol and equilibrated with a 50 μl-wash of 0.1% v/v TFA membrane. After drying their filters by centrifugation (14 000 *g*, 10 min), tips were stored at −20°C immediately before MS/MS. Peptides were eluted with 40 μl of 80% acetonitrile (ACN) in 0.1% v/v TFA, and tandem MS/MS analysis was performed on an Ultimate Ultra3000 chromatography system coupled with a Orbitrap Fusion™ Lumos™ Tribrid™ mass spectrometer (Thermo Fisher Scientific) at the Mass Spectrometry Facility of the Institute of Genetics and Cancer (IGC) of the University of Edinburgh using previously specified loading parameters [28].

Whole metabolome profiling

Five hundred microlitres of cultures in the mid-exponential growth stage were quenched by submersion into a dry ice/ethanol bath for 10 s. Samples were then spun down at 4°C (1000 *g*, 10 min) before discarding 150–450 μl from the top fraction. The remaining volume underwent an additional centrifugation (2500 *g*, 5 min) at 4°C. The resulting cell pellet was resuspended in a 10-fold volume of ice-cold HPLC-grade chloroform:methanol:water (1:3:1) mixture. An equivalent volume of 0.5 mm zirconia beads was added to the samples before they were vortexed at maximum speed for five 1-min intervals spaced by four 1-min incubations on ice. Lysates were then incubated at 4°C for 1 h with shaking at 1200 rpm. Samples were subsequently vortexed at maximum speed for 5 min on a cooled mixer before being spun down (13 000 *g*, 3 min) at 4°C to separate the cell debris from the metabolite-containing supernatants, which were stored at −80°C until they were analysed. Metabolite characterization was performed by the EdinOmics facility at the University of Edinburgh following a previously reported methodology [32].

Statistical analysis was performed using the MetaboAnalyst 5.0 [33] web-based platform, and dot plots were generated in GraphPad Prism 8.1.

Differential peak calling using DBPeaks

Raw sequencing outputs were returned as FASTQ files. Hence, after conversion into FASTA format, files were processed using the paired-end (PE) version of the pyCRAC pipeline [12, 34]. This package demultiplexes barcoded reads and removes adapter sequences by applying the previously developed Flexbar tool [35]. After filtering reads by length and nucleotide quality values (i.e. PHRED scores), the remaining reads were mapped to the reference genome using novoalign. The resulting BAM outputs were analysed by our newly developed DBPeaks.py differential peak calling script (https://git.ecdf.ed.ac.uk/sgrannem/dbpeaks). To identify differentially bound (DB) peaks, DBPeaks, the countReadsBam function of the DBPeaks script uses pyReadCounters tool from the pyCRAC package to generate GTF files with read counts and gene mapping locations. Next, the getPeaks function uses the pyCalculateFDRs script from the pyCRAC package to retrieve peaks enriched in each library relative to randomly distributed reads over the same genes. The resulting peak GTF files are then filtered by the filterPeaks function to remove peaks comprising fewer reads than the mean coverage of all the intervals in the dataset. Although we used mean, median or mean with one standard deviation can be selected as thresholds. Peak widths were normalized to a minimum length of 10 nucleotides with the adjustPeakWidths function. Afterwards, the mergeGTFintervals applied BEDTools [36] to concatenate intervals or peaks that are present in all replicates. Subsequently, the numberPeaks function assigns a number to each filtered peak to prevent misidentification in downstream steps. The software then performs a pyReadCounters analysis on the BAM files using the new GTF file encompassing the numbered filtered peaks to identify the total number of reads mapped to each peak. We then gathered the hit tables outputted by pyReadCounters and combined them using the mergeHittables function. Finally, the runDESeq function automatically performs the statistical analysis to identify differential peaks using the DESeq2 pipeline [37]. By default, DESeq2 [37] returns results in a TXT file, so we developed two additional functions to extract the calculated fold change and incorporate it into the original peak file. Finally, the getSignificantPeaks function generates a new GTF file containing solely the peaks that were called significant by the DESeq2 [37]. Given that Rpo21 recruitment is not as focalized as that of NNS, we evaluated Rpo21 changes in occupancy by conducting the mentioned differential expression analyses on the recovered reads. To compensate for possible differences in transcriptional machinery abundance, we applied a previously reported normalization strategy [38].

Microfluidics inverted microscopy image analyses

Experimental outputs were uploaded to an OMERO server [39]. To analyse the microscopy images, we used the ALIBY pipeline [40], which automates cell segmenting, tracking, and post-processing of microscopy time-lapse images. This package fetched the images from Omero and tracked the tiles constituting the traps present across time-lapse images of every position that was established during the experimental set-up. In doing so, the software accounted for any spatial drifting which may have occurred while the images were captured. The pipeline then uses the Birth Annotator for Budding Yeast (BABY) algorithm to create masks encircling the outline of the cells in the previously defined traps and subsequently tracking them across time points to generate cell lineages [41]. Cellular outlines are used to delimit the acquisitions in the brightfield and GFP channels and, consequently, extract the area, budding events, and fluorescence intensity of each cell and to estimate the volume of each cell [41]. Having computed the average fluorescence in regions laying outside cell masks, we subtracted this background from the intensity values assigned to each cell in the same image. We corrected cells too for autofluorescence by subtracting the fluorescence of cells from an untagged wild-type strain. These untagged cells were matched to the fluorescent cells both by their volume and their time of measurement. We estimated the autofluorescence using the fluorescent cell's volume and a LOWESS interpolation of the fluorescence versus volume relationship for untagged cells, recalculated in 15-min intervals. Data were visualized using seaborn and matplotlib Python libraries.

Yeast growth and fluorescence analyses

Microplate reader data was analysed using the Omniplate software [42], which processes time-series data raw outputs from microplate readers to quantify microbial growth. Omniplate blanked OD measurements by discounting absorbance signal from the wells containing media only and corrected for the non-linear relationship between OD_{600} measurements and cell count at higher absorbance values. The software then makes assumptions about the family of latent functions that can describe a population using a Gaussian-process-based algorithm [42]. In this way, Omniplate can predict errors in the estimated growth rates by fitting additional artificial replicates of the experimental data using bootstrap or iterative random re-sampling [42]. Having extracted the OD values were extracted from the triplicates for each sample, we plotted the average growth rate with an associated error corresponding to half of the interquartile range.

The getstats function computed the maximal growth rate that had been estimated based on the three technical replicates that were included for each sample [42]. To determine whether a strain was resistant or hypersensitive to oxidative challenges such as hydrogen peroxide, we calculated the logarithmic ratio of the maximal growth rate in medium containing 0.5 mM hydrogen peroxide to that of the medium lacking the reactive oxygen species. The resulting logarithmic fold changes could then be statistically compared using unpaired *t*-tests performed by GraphPad Prism 8.0.1, which was also used to generate the relevant bar plots.

For fluorescence assays, the software subtracted background fluorescent signals inherent to the media from the fluorescence readings of wells containing cells [42]. The resulting values were then corrected for autofluorescence, which was defined as the fluorescence signal emerging from an unmodified BY4741 parental strain. Final corrected fluorescence values were normalized to corrected OD_{600} measurements and plotted against time using Python's seaborn package.

Flow cytometry analyses

Experimental files were exported in their native FCS format and analysed in FlowJo 10.8.1. For cell size experiments, the normalized distribution of ungated FSC-A values was plotted in histograms. The weighted average and standard deviation were calculated for the three independent biological repeats that were assessed per cell type and condition. For cell cycle analyses and competition experiments, we introduced a gate to select for single-cell events and subsequently generated histograms of PE-Texas Red-A. To analyse DNA content in the cell cycle experiments, red fluorescence histograms were standardized to the mode of the events within all the repeats of the appropriate control strain and subsequently used to draw gates delimiting each cell cycle stage. The cell counts at each phase of the cell cycle were obtained in three independent biological repeats and used for statistical comparisons between strains. In the case of competition experiments, a gate was applied to delineate samples containing either non-red parental strain (i.e. BY4741) or the red reference (Ura7-mCherry) cells only. The counts of non-red and red cells within a competition culture were used to calculate the ratios of non-fluorescent to fluorescent cells. Given that each competition was performed in three independent repeats, a mean and standard deviation for that ratio could be determined for each strain. Non-fluorescent: fluorescent ratios and their errors were normalized to that of the pertinent reference strain and subsequently underwent a logarithmic transformation. Mutants were compared to their parental strain using unpaired *t*-tests ran in GraphPad Prism 8.1, which was also used to generate the summary histograms.

Confocal microscopy image analyses

Images were saved as CZI files and viewed with standard Image J [43] in a default stack order. Channels were split, and regions of interest (ROIs) were drawn and added to the PTM channel. Having selected the cells that were examined, we saved ROIs as ROI files for re-evaluation. In the TMRM channel, the image's stacks were *z*-projected to obtain the maximal intensity. The image's threshold was then adjusted using the Otsu's method for image segmentation, which is an algorithm for image analysis that converts fluorescence to grayscale, assigns an intensity value for every pixel and, thenceforth, partitions the latter into foreground and background based on a threshold value. All the parental replicates were assessed individually for their Otsu's optimal threshold and the highest threshold value was then imposed as a common one to discriminate between stained mitochondria and background TMRM fluorescence in all remaining images of the derived strains.

To correct for the varying background fluorescence of individual images, we specified a ROI in a space without cells and subsequently measured its fluorescence on the TMRM channel without introducing a minimal threshold. This background fluorescence was then subtracted from the mean fluorescence for the maximum projection of each selected ROI in the same image. Corrected fluorescence was then normalized to the mean corrected fluorescence of the corresponding replicate of the parental strain for direct comparison. At least 50 cells from three independent biological repeats were examined for each strain and cell line. Unpaired *t*-tests and visualization were performed in GraphPad Prism 8.1.

Respirometry analyses

Experimental traces were saved and exported in the native DLD format for analysis in the Oroboros Datlab 7 software (Oroboros). Having identified and demarcated sections on which the oxygen consumption signal remained relatively constant, we extracted the average value of these marks and used three biological replicates to calculate the mean and standard deviation for the basal respiration rates. Statistical significance was evaluated by unpaired *t*-tests performed in GraphPad 8.1, which was also used to assemble the bar plots showing the mean and standard deviation for the oxygen consumption rate of every sample across each stage.

NADH/NAD$^+$ ratio quantification

All NADH autofluorescence signals were normalized to the OD_{600} measurement in the same well. The average of the technical triplicates that were included for each sample was used as the only value for that biological replicate. Afterwards, NAD pools were calculated by subtracting the reading acquired when all NAD molecules were assumed to be oxidized (NAD$^+$) from the one at which all NAD was predominantly in its reduced state (NADH). Having estimated the NAD pool for each sample, we calculated the redox ratio of each well by discounting the background NADH fluorescence from the basal NADH measurements and dividing the resulting value over that of the NAD pool. This strategy was applied to obtain the redox ratios of three independent biological repeats per strain or cell line. Statistical analysis (unpaired *t*-tests) and visualization were performed in GraphPad Prism 8.1.

Whole transcriptome analyses

Raw sequencing outputs were returned as FASTQ files. Hence, after conversion into FASTA format, files were processed using the paired-end (PE) version of the pyCRAC pipeline [34]. This package demultiplexes barcoded reads and removes adapter sequences by applying the previously developed Flexbar tool [35]. The resulting reads undergo two quality control steps. Firstly, sequences are filtered based on their length and nucleotide quality values (i.e. PHRED scores). Secondly, since PCR artefacts will display identical random prefixes, they can easily be pinpointed and excluded from downstream analysis (collapsed). The remaining unique reads were subsequently aligned to the corresponding regions of the Saccharomyces_cerevisiae.R64-1-1.75 reference genome with the Novoalign tool (version 2.07). The pyReadCounters function of the pyCRAC package (version 1.5.2) [34] was used to compute the number of reads that map to genomic features. The resulting tables for all the samples were merged into a single TXT file that was analysed by the DESeq2 R package [37]. The pipeline corrects for size variability by computing a scaling factor for each sample [37]. To obtain such a normalization factor, the software calculates the ratio of the raw count of a given gene in one of the samples to the geometric mean of the counts for that same gene across the compared samples [37]. The median of all the ratios calculated within a sample is defined as the scaling factor for that replicate [37]. Having adjusted the raw reads, the package then performs a logarithmic transformation of the data and calculates a fold change and an FDR for each entry [37]. Statistical significance was assessed for entries which exceeded or were lower than log2 fold change of 1 and −1, respectively [37], and had an FDR value of 0.05 or less.

Proteomics analyses

Raw data were processed using MaxQuant version 1.6.5.0 with the Andromeda search engine [44, 45] for peptide identification. Inputs included a CSV file detailing the experimental design, a FASTA database (UP000002311 559 292 YEAST *Saccharomyces cerevisiae*), and RAW files. Trypsin was used as the protease, with a minimum peptide length of seven amino acids, allowing up to two missed cleavages. Initial peptide tolerance was set at 20 ppm, reduced to 4.5 ppm for main searches, with a peptide spectrum match (PSM) threshold of 1% FDR for statistical significance. Cysteine carbamidomethylation was a fixed modification, while methionine oxidation and protein N-terminal acetylation were variable modifications.

Post-analysis, MaxQuant outputted a proteinGroup TXT file, which was adjusted to include only intensity columns for comparison sets. This matrix was analysed using Perseus [46] for statistical evaluation, filtering out PTMs, reverse proteins, and contaminants. Intensities were log-transformed, and proteins not detected in at least two replicates per strain were excluded. Missing values were imputed using a downshifted normal distribution. Statistical analysis of the log2-transformed data was conducted using EdgeR [47], which performed differential expression analysis. Significant changes were defined by fold changes >1 or <-1, indicating a two-fold difference in expression relative to the parental strain.

Gene ontology analyses

Biological processes enrichment analysis was performed using PANTHER (Protein ANalysis THrough Evolutionary Relationships) [48]. For transcriptomic assessment, RNAs displaying a 2-fold differential expression were used as input for the analysis. For proteomic evaluation, all significantly differential factors were fed to the PANTHER software. In the latter case, fold thresholds were omitted to provide a sufficiently large sample size from which the PANTHER suite could draw statistical conclusions on enriched GO terms. Bar plots were generated in GraphPad Prism 8.1.

Results

Mutating NNS-binding sites in *PIC2* elevates its expression

To quantitatively monitor levels of Pic2, we used a strain in which *PIC2* was expressed as a C-terminal GFP-fusion protein (*Pic2–GFP*). We subsequently used CRISPR–Cas9 gene editing to introduce silent point mutations in previously reported *PIC2* NNS-binding sites [12] (Fig. 1B and Supplementary Fig. S1). We engineered two mutants: one without Nab3-binding sites in *PIC2* (mut-Nab3-BS) and another without both Nrd1 and Nab3 binding sites (mut-NNS-BS; Fig. 1B). We expected that blocking NNS binding within the first 500 bp downstream of the *PIC2* transcription start site (Fig. 1B) would prevent its premature termination during transcription and increase *PIC2* mRNA and protein levels. *PIC2*, which encodes a mitochondrial copper and phosphate transporter important for respiration [13, 14], is downregulated during fermentation [12]. Thus, we supplemented growth media with high (2%) or low (1%) concentrations of the poorly fermentable sugar raffinose. In raffinose, cells respire and, therefore, should upregulate *PIC2* expression. Consistently, RT-qPCR analyses on RNA extracted from yeast grown in raffinose and in glucose confirmed that *PIC2* expression is substantially higher in raffinose (Fig. 1C).

We next determined whether altering NNS binding to *PIC2* indeed increased its mRNA abundance. RT-qPCR revealed that *PIC2* mRNA levels increased by 2- to 4-fold in mut-Nab3-BS compared to its parental strain (Fig. 1D and E), consistent with defective premature transcription termination of *PIC2*. The mut-NNS BS mutant also showed significantly increased steady-state levels, albeit slightly lower compared to mut-Nab3-BS (Fig. 1D and E). Since this upregulation was highest in lower raffinose concentrations (Fig. 1E), we performed subsequent experiments in 1% raffinose.

Nrd1 binding to *PIC2* mRNA can be independent of Nab3 binding to the transcript

To confirm that the mutations introduced in *PIC2* indeed impeded NNS binding, we mapped Nab3 and Nrd1's transcriptome-wide occupation in the parental and mutant *Pic2–GFP* strains using the CRACs method [20, 27] (Supplementary Fig. S2A and B). To complement these analyses, we also performed RNA-seq on these strains to quantify changes in RNA steady-state levels. Additionally, CRAC with Rpo21 was performed to monitor the impact of these mutations on Pol II occupancy on *PIC2*. To identify statistically significant changes in the NNS-binding profiles, we developed DBPeaks, a Python peak-calling script that employs pyCRAC [34], BEDTools [36, 49], and DESeq2 [37] to detect DB peaks among CLIP/CRAC datasets (Supplementary Fig. S2A and tracks showing differential peaks; Fig. 1F). As expected, disrupting both Nrd1- and Nab3-binding sites (mut-NNS-BS) almost completely abrogated the binding of both proteins to the *PIC2* transcript. The mut-Nab3-BS mutations blocked Nab3 binding to *PIC2*, as hypothesized, but a fraction of Nrd1 cross-linking is still retained throughout its binding sites. These data demonstrate that Nrd1 can still be recruited to *PIC2* even when Nab3 binding to the transcript is abolished.

Impeding Nab3 binding to *PIC2* mRNA significantly alters its half-life but not *PIC2* RNA polymerase occupancy

Analysis of the RNA-seq and Pol II CRAC data revealed that while *PIC2* mRNA steady-state levels significantly increased, Pol II occupancy on the gene was not significantly altered (Fig. 1F; Rpo21 CRAC). Globally, Pol II CRAC signals were not significantly different in the mut-Nab3-BS strain (Supplementary Table S8). Based on these data and that effective release of NNS requires degradation of the target RNA [50], we hypothesized that Nrd1 and, perhaps, Sen1 remain bound to *PIC2* mRNA post-transcriptionally and that their increased retention time impedes *PIC2* mRNA degradation. To test this, we quantified the mRNA decay rates of *PIC2* in the *Pic2–GFP* strain and its two mutants upon transcription inhibition using thiolutin. This assay revealed that the half-life of *PIC2* mRNA in the mut-Nab3-BS strain was almost double (19.1 min; Supplementary Fig. S3) that of parental *Pic2–GFP* reference (10.8 min; Supplementary Fig. S3). While the mut-NNS-BS mRNA levels increased ∼2-fold in 1% raffinose (Fig. 1E), the mutations did not significantly change *PIC2* mRNA half-life (Supplementary Fig. S3B and C). These results indicate that preventing Nab3 binding specifically stabilizes *PIC2* mRNA.

Table 1. Summary of the key findings of the RNA-seq, MS/MS and CRAC experiments

RNA-seq	Total transcripts	Differentially expressed transcripts	Upregulated	Downregulated
mut-Nab3-BS	12 411	488 (3.9%)	196(98 mRNAs, 97 ncRNAs, 1 rRNA)	292(266 mRNAs, 25 ncRNAs, 1 tRNA)
mut-NNS-BS	12 411	41 (0.1%)	31(14 mRNAs, 17 ncRNAs)	10(9 mRNAs, 1 ncRNA)
Mass spectrometry	Total proteins	Differentially expressed proteins	Upregulated	Downregulated
mut-Nab3-BS	1056	94 (9%)	56	38
mut-NNS-BS	1056	50 (4.7%)	38	12
Nab3 CRAC	Total peaks	Differentially bound Nab3 peaks	More Nab3 binding	Less Nab3 binding
mut-Nab3-BS	17 643	6 (0.03%)	4	2 (including *PIC2*)
mut-NNS-BS	17 270	1 (0.006%)	0	1 (only *PIC2*)
pTEF1-PIC2	12 464	647 (5.19%)	290	356
*pic2*D	13 340	300 (2.25%)	117	184
Nrd1 CRAC	Total peaks	Differentially bound Nrd1 peaks	More Nrd1 binding	Less Nrd1 binding
mut-Nab3-BS	37 368	378 (1%)	24	354
mut-NNS-BS	41 492	442 (1.2%)	10	432
pTEF1-PIC2	12 992			
Rpo21 (Pol II) CRAC	Total RNAs	Differentially bound ncRNAs and mRNAs	More Rpo21 binding	Less Rpo21 binding
mut-Nab3-BS	12 421	0 (0%)	0	0
mut-NNS-BS	12 421	102 (0.82%)	70	32

Disrupting Nab3 binding to *PIC2* mRNA alters Nrd1 binding to other NNS targets

If our hypothesis is correct and Nrd1 and Sen1 indeed have a prolonged retention time on the mut-Nab3-BS transcript, then this may reduce their availability and alter their binding to their usual targets. In particular, Sen1 appears to be a limiting factor for the assembly of the complex (Supplementary Table S9) [51]. Our hypothesis was based on previous work [50] demonstrating that overexpressing a degradation-resistant circular ncRNA decoy that contained multiple NNS-binding sites altered Nrd1 and Nab3 occupancy across the transcriptome. However, a caveat with our model is that contrary to the circular decoy RNA, *PIC2* is lowly abundant, and the modest increase in *PIC2* transcript levels in the mut-Nab3-BS strain begs the question whether this mRNA pool could effectively sequester sufficient NNS components to have any impact on the transcriptome or cause any distinct phenotypes in this mutant.

To answer this question, as a first step, we conducted RNA-seq and proteomics analyses on *Pic2–GFP* and mut-Nab3-BS (Table 1) to determine if the mutations caused any changes in genes regulated by NNS. While no significant changes Pol II occupancy could be detected in the mut-Nab3-BS strain (Table 1), 488 transcripts were significantly differentially expressed (DE; ∼4% of detected RNAs) in the RNA-seq data. This implies that, similar to *PIC2,* not the transcription of these genes, but their mRNA stability is affected. Ninety-two proteins (9% of all identified factors) were also DE in mut-Nab3-BS (Fig. 2A and B). In contrast, mut-NNS-BS, which was only expressed at ∼2-fold higher levels than *Pic2–GFP* showed changes in only 41 transcripts and 50 proteins (0.1% and 4.7% of totals; Table 1). Over 60% of the DE transcripts in mut-Nab3-BS were also found to be bound by Nrd1 and Nab3 in our CRAC data (Fig. 2A). Of these transcripts, ∼20% were non-coding RNAs, including numerous CUTs, while ∼40% were protein-coding. Similarly, >40% of the DE proteins in mut-Nab3-BS were identified as putative NNS targets in our CRAC datasets. Nrd1 and Nab3 RNA recognition motifs (RRMs) were also significantly more prevalent among the DE transcripts in mut-Nab3-BS compared to those in the entire transcriptome. Importantly, none of the NNS components were significantly DE in our transcriptomic datasets (Supplementary Table S10). Furthermore, western blot analyses on lysates from cells grown in 1% raffinose also did not show strong changes in NNS protein levels (Supplementary Fig. S4).

To confirm that the observed changes in the transcriptome and proteome were indeed driven by altered Nab3 and Nrd1 binding to NNS targets, we employed our DBPeaks tool to identify DB Nab3 and Nrd1 peaks within the CRAC datasets (Table 1). Mutations in the Nab3 motifs of *PIC2* did not significantly affect global Nab3 binding (Table 1). In contrast, Nrd1 binding was significantly altered in both mutants, with hundreds of DB Nrd1 peaks identified (representing 1% of all detected peaks; Fig. 2D and Table 1). Consistent with reduced Nrd1 availability, most of the 378 DB Nrd1 sites in mut-Nab3-BS exhibited less Nrd1 binding (Table 1). Although Nrd1 autoregulates its own expression [52], the *NRD1* transcript was not DB by Nrd1 or Nab3 (Supplementary Fig. S5), implying that the observed changes in Nrd1 binding were not sufficient to impact its own expression. More than 10% of the DB Nrd1 sites [41] were in DE genes (Fig. 2D and Table 1), such as *DUR3,* a stress-specific mRNA known to be regulated by the NNS complex [12] (Supplementary Fig. S6). Similarly to *DUR3,* reduced Nrd1 binding predominantly occurred in regions annotated to contain pervasive transcripts (e.g. CUTs) upstream of protein-coding genes (Fig. 2E). However, over 60% of the upregulated RNAs of mut-Nab3-BS exhibited decreased Nrd1 binding to their coding sequence (Fig. 2E, and Supplementary Figs S7 and S8), suggesting that

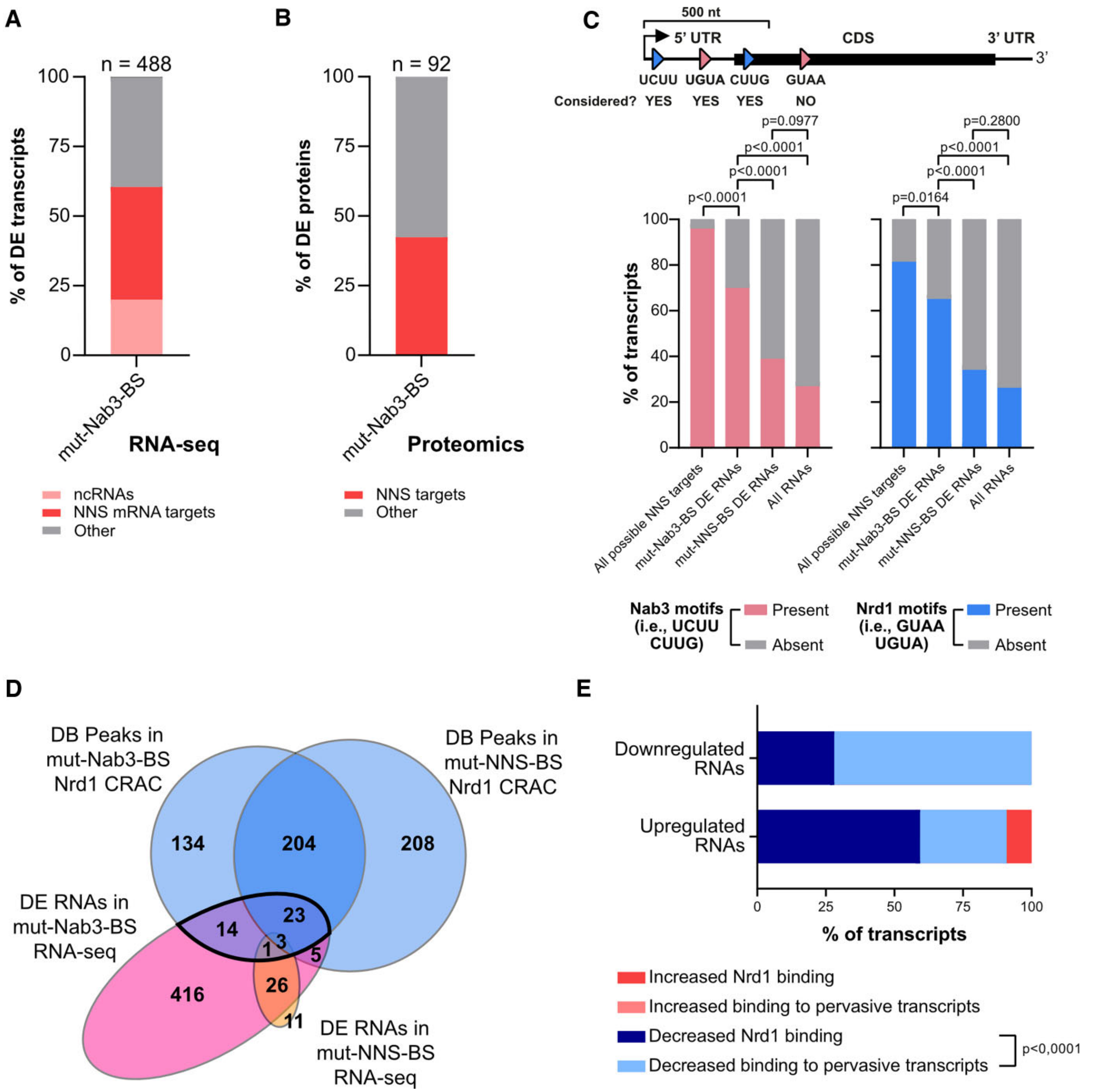

Figure 2. Disrupting Nab3 binding to *PIC2* prompts an accumulation of NNS targets at a transcriptomic and proteomic level. (**A** and **B**) Stacked bar charts showing the proportion of DE RNAs and proteins in mut-Nab3-BS bound by Nab3 and Nrd1 in our CRAC data. Panel (A) also indicates the portion of DE transcripts comprising ncRNAs. (**C**) Fraction of transcripts containing Nab3- and Nrd1-binding motifs across DE transcripts of the mut-Nab3-BS and mut-NNS-BS strains, all transcripts annotated in the genome (negative control, "All RNAs") and all transcripts with at least one Nrd1 or Nab3 motif (positive control, "All possible NNS targets"). As shown in the schematic, the analysis only considered Nrd1 or Nab3 motifs within the first 500 nucleotides downstream of the gene start site. *P*-values were calculated using a Fisher's exact test. (**D**) Venn diagrams showing overlaps between the DE transcripts and the DB Nrd1 peaks in mut-Nab3-BS and mut-NNS-BS. RNAs that are DE and DB by Nrd1 in mut-Nab3-BS are itemized in (**E**). (E) Stacked bar charts displaying the nature of the change of the DB Nrd1 peaks (increased or decreased) across DE RNAs (upregulated or downregulated) in the mut-Nab3-BS strain. DB peaks lay directly within the first 500 nucleotides of the DE RNA or were detected within a pervasive transcript expressed just upstream of the DE RNA). *P*-values were calculated using a Fisher's exact test and reported on the plot.

their abundance increases due to defective NNS recycling and degradation of the mRNA.

While mut-NNS-BS also exhibited numerous DB Nrd1 peaks, these changes did not impact the transcriptome and proteome as much as compared to mut-Nab3-BS, as evidenced by the fewer DE genes (Fig. 2D and Table 1). Additionally, its DE transcripts were not significantly enriched for Nrd1 and Nab3 motifs (Fig. 2C), suggesting that their altered expression is not linked to altered NNS activity. Therefore, although both mutants demonstrated altered Nrd1 binding, the resulting transcriptomic and phenotypic consequences were markedly different.

One important piece of data that was missing was a global analysis of Sen1 occupancy in the *Pic2–GFP* reference and its mutant strains. We indeed performed CRAC experiments with a strain expressing a C-terminally HTF-tagged Sen1. Unfortunately, under the growth conditions used, Sen1 was lowly expressed and cross-linking to RNA was inefficient relative to the other NNS components (Supplementary Fig. S2B). Despite multiple attempts, the resulting Sen1 CRAC cDNA libraries were of too low complexity (but are publicly available; see Data availability) to draw any conclusions confidently. As an alternative approach to CRAC, we applied RNA immunoprecipitation (RIP) assays in the parental and mutant *Pic2–GFP* strains. Briefly, we affinity-purified Sen1-bound RNAs (without prior cross-linking) and used RT-qPCR to quantify *PIC2* enrichment relative to RNA extracted from total lysate samples (input controls; Fig. 3) as well as several other known NNS targets. This revealed that Sen1 association with the mut-Nab3-BS *PIC2* transcript, when normalized to the amount of transcript present in the corresponding lysate, was four times higher compared to the parental *Pic2–GFP* transcript. Sen1 co-precipitation of the mut-NNS-BS *PIC2* mRNA was also detected, but this was not significantly higher compared to its *PIC2* mRNA abundance. We could not detect a significant enrichment of the reference mRNA (i.e. *ALG9*; Fig. 3B) and two other NNS targets (i.e. *NEL025c* and *SNR13*; Fig. 3C and D) among the Sen1 co-precipitated RNAs in both mutant strains, suggesting that not all NNS targets show enhanced Sen1 binding.

Collectively, the observed changes in Nrd1 binding in the CRAC data, combined with the Sen1 RIP experiment, support our model that NNS components are sequestered on the *PIC2* transcripts lacking Nab3-binding sites.

Abrogating Nab3 binding to *PIC2* decreases fitness, enlarges cell size, and delays cell cycle progression

A key question we next addressed was the biological implications of these mutations. We hypothesized that if NNS regulation of *PIC2* expression is functionally important, then impairing *PIC2* regulation by NNS should result in measurable phenotypic consequences. To test this, we first quantified the maximum growth rates of the *Pic2–GFP*, mut-Nab3-BS, and mut-NNS-BS strains (Fig. 4A). This revealed that removing Nab3-binding sites in *PIC2* caused growth defects in low raffinose medium. Upon microscopic inspection of the mut-Nab3-BS cells (Fig. 4B), we noticed that these cells were visibly larger than the parental *Pic2–GFP* strain. Similar cell size changes were observed in strains where NNS components were depleted/inactivated; however, these observations were not further analysed [53–55]. We next compared cell sizes across all strains using flow cytometry. The average cell size of mut-Nab3-BS cells was ∼50% larger than that of the parental strain, while mut-NNS-BS showed no significant size increase (Fig. 4C and D). Given the modest increase in *PIC2* mRNA levels in the mut-Nab3-BS mutant, this phenotype was particularly striking. To substantiate these findings, we used microfluidics and time-lapse microscopy to quantify cell size and Pic2–GFP expression levels in single cells for both parental and mutant strains, including a non-fluorescent parental control to correct for autofluorescence [40, 41]. Consistent with our flow cytometry data, the microfluidics analysis confirmed that mut-Nab3-BS cells had markedly larger cell volumes and broader cell volume distributions compared to the parental strain (Fig. 4E).

Interestingly, quantification of Pic2–GFP fluorescence in individual cells from the microfluidics revealed that both mutant strains exhibited higher mean fluorescence and greater cell-to-cell variability in Pic2–GFP concentration (Fig. 4F; cell mean fluorescence). This shows that completely or partially disrupting NNS regulation increases cell-to-cell heterogeneity in Pic2–GFP concentration.

We conclude that NNS regulation of *PIC2* is important not only for maintaining appropriate cell volumes but also for ensuring more homogeneous Pic2 protein concentrations across the cell population. This finding suggests a potential novel role for the NNS pathway in reducing cell-to-cell variability in protein concentration (see Discussion).

Before further exploring this phenotype, we sought to ensure that the observed cell size increase was indeed genetically linked to the mutations we introduced to disrupt NNS regulation of *PIC2* and not due to any CRISPR-related off-target effects. Fluorescent strains were backcrossed with a non-fluorescent strain of the opposite mating type (BY4742). After undergoing meiosis and sporulation, the resulting diploid strain yielded tetrads enclosing four haploid daughter cells (Supplementary Fig. S9A). Among these, two encoded a wild-type version of *PIC2,* and the remaining ones expressed the *GFP*-tagged *PIC2*. Upon tetrad dissection, cell size measurements confirmed that haploids carrying the mut-Nab3-BS mutations were also larger than their non-fluorescent counterparts. Accordingly, we conclude that the increased cell size co-segregated with the disruption of NNS regulation of *PIC2*.

To substantiate this control experiment, we studied additional independently derived mutant clones. After performing RT-qPCR analyses and cell size measurements on a second mut-Nab3-BS clone (Nab3 BS #2; Supplementary Fig. S9B), we observed comparable increases in *PIC2* mRNA levels (Supplementary Fig. S9C) and cell size (Supplementary Fig. S9D and E). When screening for additional mut-NNS-BS clones, we serendipitously identified a strain that lacked all Nab3 binding sites and half of the Nrd1 motifs (Supplementary Fig. S9B; partial mut-NNS-BS). This mutant exhibited intermediate increases in *PIC2* mRNA levels (Supplementary Fig. S9C) and cell size (Supplementary Figs. S9D and E). Hence, these findings suggest that the extent of *PIC2* upregulation and the accompanying cell size enlargement was (at least in part) dictated by the number of intact Nrd1 motifs present in *PIC2,* together with the absence of Nab3-binding sites.

Earlier work has established that cell cycle progression is prolonged in oversized cells [56]. Therefore, we analysed

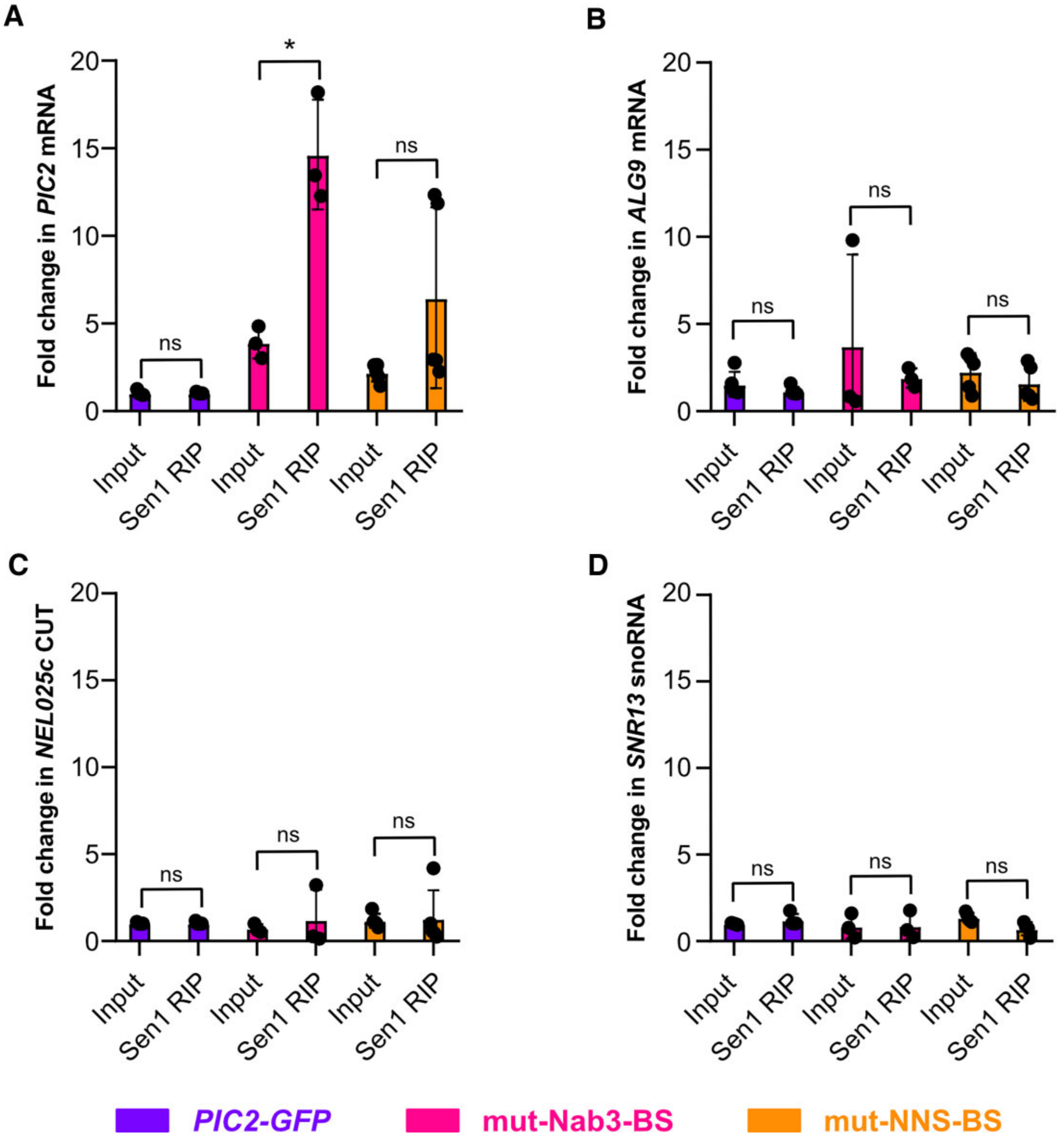

Figure 3. Abolishing Nab3 recognition sequences in *PIC2* increases Sen1 binding to *PIC2* mRNAs. (**A–D**) Fold changes of *PIC2, ALG9, NEL025c,* and *SNR13* RNA levels in the transcriptome and Sen1 co-immunoprecipitated fractions of the mut-Nab3-BS and mut-NNS-BS mutants, respectively, compared to the parental strain. Cells were grown in SC -Ura supplemented with 1% (w/v) raffinose. Bar plots display means and SDs of three independent biological repeats. *P*-values were calculated using a two-tailed paired Student's *t*-test.

the cell cycles of the parental and mutant *Pic2–GFP* strains using flow cytometry and propidium iodide dye to stain DNA. Notably, a greater portion of the mut-Nab3-BS populations were in S or G2/M phases (Fig. 4G and H, and Supplementary Figs. S9F and G). Thus, our results revealed a mild cell cycle prolongation in strains lacking *PIC2* Nab3-binding sites. Moreover, a modest increase in the fraction of polyploid cells was also observed in mutant strains, suggesting a higher rate of mitotic defects. In line with our cell size measurements, the partial NNS mutant (partial mut-NNS-BS) showed intermediate cell cycle delays, and no defects were detectable in the strain lacking all NNS-binding sites in *PIC2* (mut-NNS-BS; Fig. 4G and H, and Supplementary Fig. S9F and G).

Collectively, these data show that the observed increases in *PIC2* transcript and protein levels, caused by specifically disrupting Nab3 binding to *PIC2*, result in abnormal cell size and delays in cell cycle progression.

Impeding Nab3 binding to *PIC2* causes mitochondrial hyperpolarization and resistance to oxidative stress

We next sought to elucidate to what extent the growth defects of mut-Nab3-BS in low raffinose medium were linked to the increased expression and activity of Pic2. We first measured mitochondrial membrane potential ($\Delta\psi_m$), a major index of mitochondrial energy homeostasis. Live cells were equilibrated with TMRM, a dye that accumulates in active mitochondria proportionally to their activity. Subsequent live cell confocal microscopy revealed mitochondrial membrane hyperpolarization in the mut-Nab3-BS mutant (Fig. 5A). Increased mitochondrial membrane potential can stem from enhanced respiratory rate or inhibited ATP synthesis, but the latter would cause a decreased respiratory rate. Hence, to further interpret these findings, we quantified oxygen consumption. This revealed that respiratory rate was significantly increased in mut-Nab3-BS compared to the parental *Pic2–GFP*

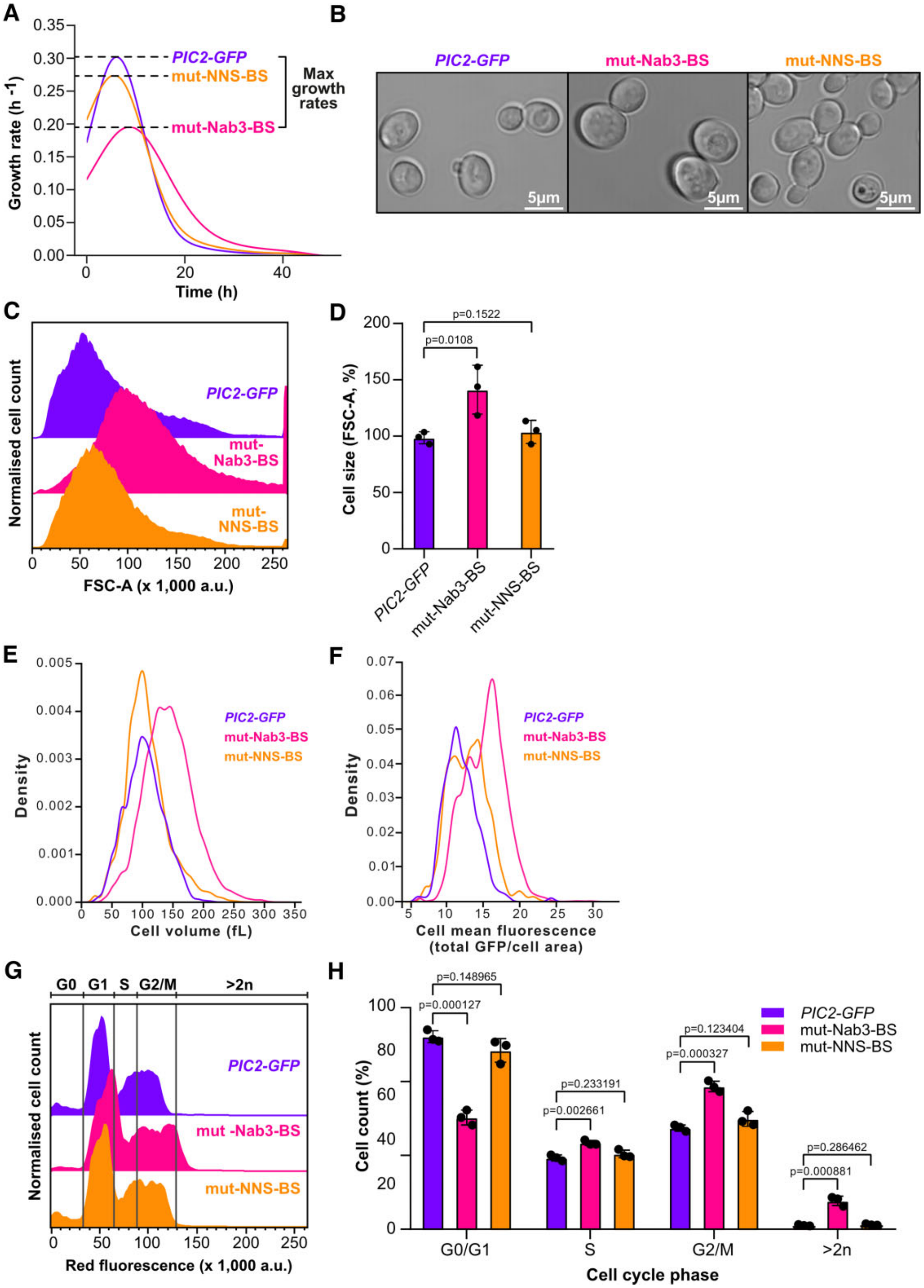

Figure 4. Preventing Nab3 binding to *PIC2* causes growth defects, increases cell size, enhances Pic2–GFP expression, and delays cell cycle progression. (**A**) Time-resolved growth rates of the *Pic2–GFP*, mut-Nab3-BS, and mut-NNS-BS strains. The mean growth rate was estimated by Omniplate based on three technical replicates. Maximum growth rates for each strain are indicated. (**B**) Confocal bright-field images of *Pic2–GFP*, mut-Nab3-BS, and mut-NNS-BS strains. mut-Nab3-BS are visibly larger. (**C**) Representative traces of the cell size distribution of *Pic2–GFP* and derived mutants from flow cytometry analyses. The sizes were compared using their forward light scatter (FSC-A) values. mut-Nab3-BS cells are larger. (**D**) Weighted means and SDs of the median FSC-A values for three independent biological repeats calculated for each strain and normalized to the parental *Pic2–GFP* strain. (**E**) Distribution of cell volumes (in fL) for the *Pic2–GFP*, mut-Nab3-BS, and mut-NNS-BS strains, calculated using the microfluidics imaging data. (**F**) Distribution of mean cell Pic2–GFP fluorescence, calculated by dividing the Pic2 fluorescence (arbitrary units) of each cell by its area. Accounting for the larger size of the mut-Nab3-BS mutant, the concentration of GFP is still higher. (**G**) Representative flow cytometry traces of cells with fluorescently marked DNA of *Pic2–GFP*, mut-Nab3-BS and mut-NNS-BS strains at mid-log phase (OD_{600} ∼0.5). (**H**) Weighted means and SDs of the population fraction of each strain in (E) within each cell cycle phase. Values are based on biological triplicates. All *P*-values in the figure were calculated using a two-sided unpaired Student's *t*-test.

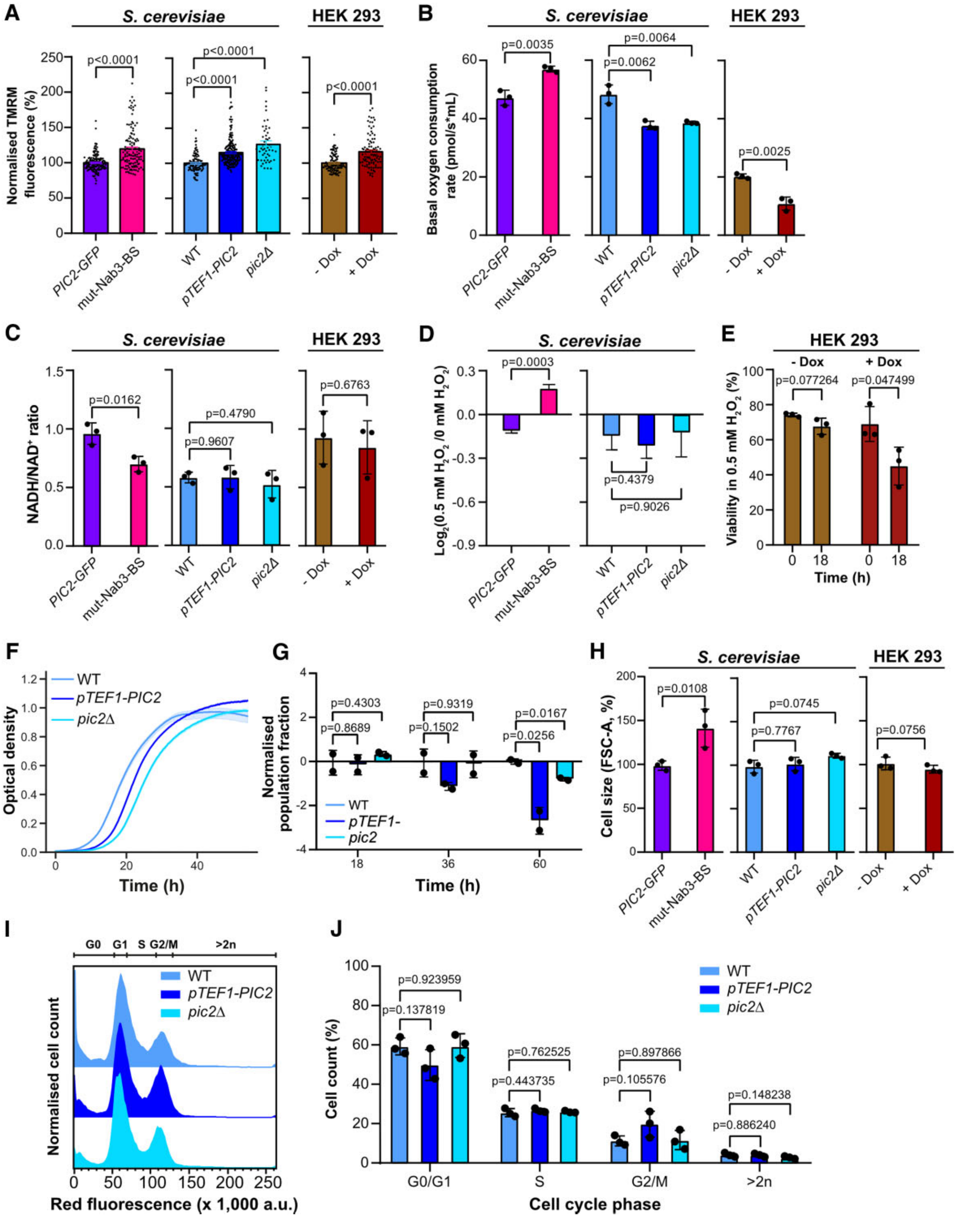

Figure 5. Overexpression of Pic2 decreases yeast and mammalian cell fitness but affects neither cell size nor cell cycle. (**A**) Mean and SEM for TMRM fluorescence values, indicating mitochondrial membrane potential, gathered from confocal imaging of more than 50 cells from three different biological repeats. *P*-values were calculated using a two-sided Mann–Whitney *U* test. (**B**) Mean and SD for basal oxygen consumption rates measured in biological triplicates. *P*-values were calculated using a two-sided unpaired Student's *t*-test. (**C**) Mean and SD for NADH/NAD$^+$ ratios recorded in three independent assays. *P*-values were calculated using a two-sided unpaired Student's *t*-test. (**D** and **E**) Mean and SD of the log$_2$-transformed fold change in the growth rate of cells grown with and without the presence of 0.5 mM hydrogen peroxide in the medium. Measurements were performed in a microplate reader. For HEK 293 cells (E), the mean and SD of live cells are shown. Trypan blue assays were performed in three independent samples. *P*-values were calculated using a two-sided unpaired Student's *t*-test. (**F**) Time-resolved optical density measurements depicting the mean and with shading half the interquartile range of three technical repeats. WT displayed the shortest lag phase. (**G**) Weighted means and SDs of the cell size (FSC-A values in flow cytometry) for three independent biological repeats were calculated for each cell type and normalized to that of the pertinent reference. *P*-values were calculated using a two-sided unpaired Student's *t*-test. (**H**) Log$_2$-transformed fold changes of the population fraction of tested strains (i.e. WT, *pTEF1-PIC2*, and *pic2Δ*) against a fluorescent reference. Values shown are averages and SDs from biological triplicates and were normalized to the fold changes observed in the parental strain. (**I**) Representative flow cytometry traces of the DNA profile of *pTEF1-PIC2*, *pic2*D, and their parental strain (WT). (**J**) Weighted means and SDs of the population fraction of each strain in (H) undergoing each cell cycle phase. *P*-values were calculated using a two-sided unpaired Student's *t*-test.

in low raffinose concentrations (Fig. 5B) and suggested that this increased rate drives the higher mitochondrial membrane potential.

Based on these data and on previous work reporting that oversized cells undergo continual stress responses [56], we hypothesized that the observed defects in mitochondrial energy homeostasis arose from intracellular stress. To test this, we quantified the nicotinamide adenine dinucleotide (NAD) pools of both strains by performing UV fluorescence assays in a microplate reader. Consistent with increased respiration and enhanced ROS production, NAD species in mut-Nab3-BS were predominantly in their oxidized NAD^+ state compared to the parental strain (Fig. 5C). Furthermore, to corroborate that mut-Nab3-BS was inherently stressed, we devised an oxidative stress assay based on acquired stress resistance: since exposure to a mild insult confers some resistance to subsequent ones, we expected stressed cells to be less affected by environmental challenges. Indeed, whereas the growth of the parental strain was reduced by exposure to hydrogen peroxide, that of mut-Nab3-BS did not decrease (Fig. 5D).

We conclude that disrupting Nab3 binding to *PIC2* mRNA causes energy homeostasis anomalies that generate greater respiratory demands and intracellular oxidative stress.

Pic2 overexpression alters Nab3 binding transcriptome-wide but does not recapitulate all the phenotypes observed in mut-Nab3-BS

We next investigated the mechanism underlying the observed defects in growth, cell size, cell cycle, and energy homeostasis. The simplest explanation was that these phenotypes resulted from increased *PIC2* mRNA abundance, which would lead to elevated Pic2 protein levels and activity. It is possible that the cellular stress caused by increased Pic2 levels induced gene expression changes that contribute to the observed redistribution of NNS proteins on their targets. Hence, we predicted that overexpressing Pic2 in low raffinose medium should (i) cause similar redistribution of NNS components and (ii) exacerbate or at least reproduce these cellular defects. To address this, we generated both a *PIC2* overexpression strain (*pTEF1-PIC2*; Supplementary Fig. S10A; Fig. 5) and a knockout strain (*pic2*Δ; Fig. 5), including versions with HTF-tagged Nab3 to monitor NNS recruitment changes using CRAC. The *pTEF1* promoter increased *PIC2* mRNA levels over 1000-fold on average (Supplementary Fig. S10A) and significantly increased Nab3 cross-linking to *PIC2* mRNA (∼3.5-fold; Supplementary Fig. S10B). The *PIC2* knockout strain showed no detectable Nab3 binding to its transcript, as expected. Nab3 CRAC data revealed numerous DB Nab3 peaks in both strains, confirming that either increased or decreased *PIC2* expression can indeed redistribute Nab3 (Supplementary Fig. S10C).

Phenotypic analysis showed that both mutants recapitulated some defects observed in mut-Nab3-BS. Consistent with previous work, the *pic2*Δ mutant exhibited growth defects in low raffinose medium, with delayed entry into exponential phase (Fig. 5F). *PIC2* overexpression caused comparable growth delays (Fig. 5F), and competition assays confirmed fitness costs for both mutants (Fig. 5G). Both *PIC2* knockout and *PIC2*-overexpressing strains displayed mitochondrial hyperpolarization like mut-Nab3-BS (Fig. 5A). However, the underlying mechanism differed: basal oxygen consumption was reduced in both *pic2*Δ and *pTEF1-PIC2* strains (Fig. 5B), but neither showed significant NADH/NAD+ changes nor oxidative stress resistance (Fig. 5C and D). The combination of increased mitochondrial membrane potential with decreased respiratory rate suggests inhibited ATP synthesis, potentially caused by altered phosphate homeostasis in the *PIC2* overexpression model.

Crucially, while Pic2 overexpression or deletion recapitulated some mut-Nab3-BS phenotypes, these mutants were not significantly larger than their parental counterpart (Fig. 5H) and showed no significant cell cycle progression defects or delays (Fig. 5I and J).

We conclude that the cell size and cell cycle phenotypes are specifically linked to disrupting Nab3 binding to *PIC2*, rather than simply altering Pic2 protein levels.

Blocking Nab3 binding to *PIC2* increases cell size and delays cell cycle progression

Previous studies [53–55] also observed cell size increases in mutants in which Nab3, Nrd1, or Sen1 were conditionally depleted. However, this phenotype was not further analysed in these studies. To verify these findings, we employed a strain in which Nab3 could be conditionally depleted from the nucleus in the presence of rapamycin [12, 57] (*NAB3-FRB*; Fig. 6A) with the parental strain (WT) as a negative control (Fig. 6B). Using flow cytometry, we monitored cell size at 1, 4, and 8 h after adding rapamycin. Cell size steadily increased after 4 h of rapamycin treatment, and after 8 h of exposure to the drug, it became equivalent to that observed in mut-Nab3-BS. Treating the parental strain with rapamycin for 8 h resulted in minor increases in cell size (Fig. 6A and Supplementary Fig. S11A). Rapamycin can arrest cells in G1 [58], ultimately increasing their cell size [56]. Thus, although engineered to resist the toxicity of rapamycin [57], the parental strain does not appear to be completely insensitive to the drug. We also performed time-resolved cell cycle analyses in the Nab3-depleted mutant and its parental strain (Fig. 6C and Supplementary Fig. S11). Since yeast doubles every 3.5 h in low raffinose medium, we extended the timespan of the experiment to encompass several cell cycles through which the oversized mutant was expected to become delayed. Indeed, 16 h after sequestering Nab3 in the cytoplasm, cells spent less time in G1, underwent prolonged S phases and became polyploid more frequently than their parental counterparts (Fig. 6C and Supplementary Fig. S11B). These effects aggravated after 32 h, when significantly longer S phases were replaced by extended G2/M phases, reminiscent of cell cycle changes in the mut-Nab3-BS strain. As anticipated, rapamycin eventually also arrested the parental strain in G1 [58], thereby gradually shifting its population towards 1n states throughout the experiment.

These data confirm that nuclear depletion of NNS components (Nab3 in this case) can cause increased cell size and aberrant cell cycle progression. Remarkably, these phenotypes mirror those observed in the mut-Nab3-BS strain, even though mut-Nab3-BS contains only two single-nucleotide substitutions that disrupt Nab3 binding to a single mRNA target. This striking similarity suggests that the NNS regulatory system is highly sensitive to even minor changes in NNS binding to their targets.

To understand the broader cellular consequences of disrupting Nab3 binding to *PIC2*, we conducted gene ontology analyses on the DE transcripts and proteins of mut-Nab3-BS (Supplementary Fig. S12A and B). Consistent with

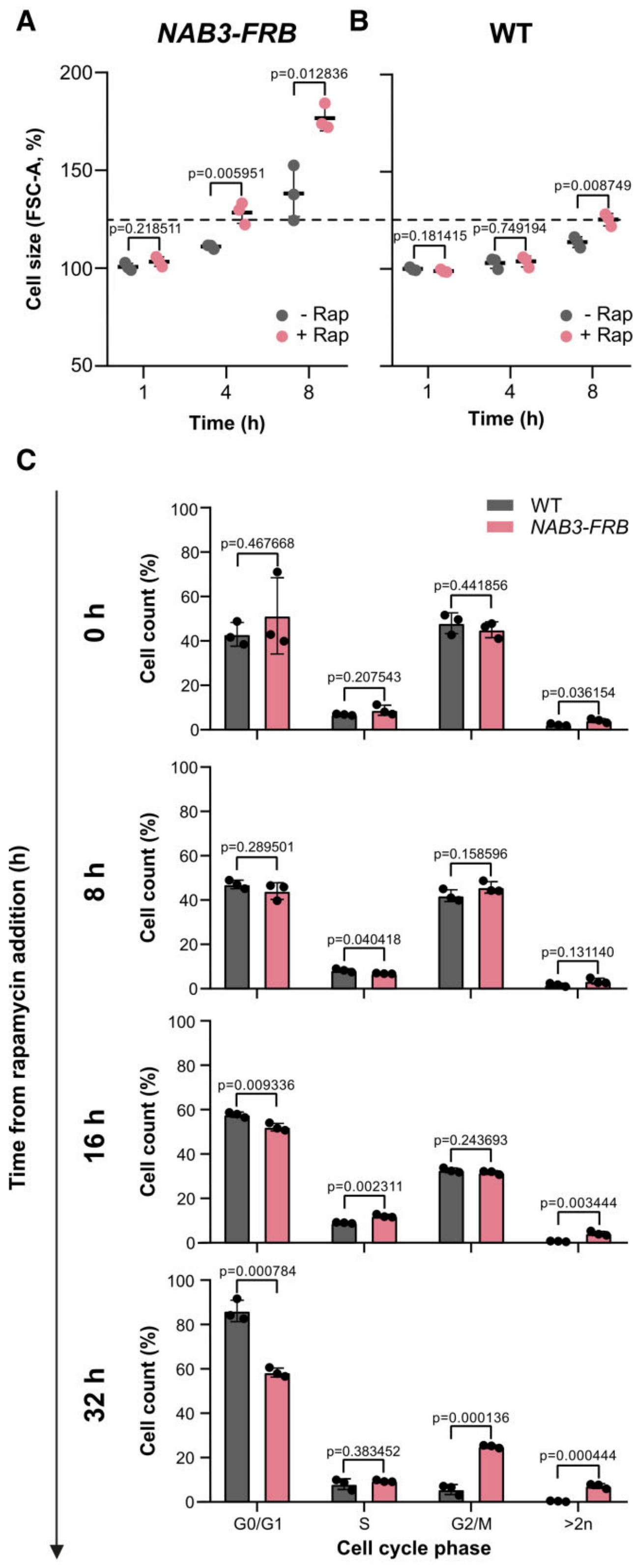

Figure 6. Depleting Nab3 from the nucleus increases cell size and prolongs the cell cycle. (**A** and **B**) Time-resolved means and SDs of cell size medians from three independent evaluations of *NAB3-FRB* and its parental strain (WT). The resulting values were normalized to that of the untreated reference collected in the first time point. (**C**) Bar plots displaying weighted means and SDs of the population fraction of *NAB3-FRB* and its WT control within each cell cycle phase. All *P*-values were calculated using a two-sided unpaired Student's *t*-test.

the excessive cell size of the mut-Nab3-BS mutant, both translation and transcription processes were downregulated [56] (Supplementary Fig. S12A and B). The downregulation of transcripts involved in cell cycle regulation may explain the delayed transition of mut-Nab3-BS through the G2/M phase (Supplementary Fig. S12A). Moreover, the upregulation of responses to nutrient, oxidative, and copper stress suggests higher levels of intracellular stress in mut-Nab3-BS and, accordingly, increased tolerance to extracellular ones (Supplementary Fig. S12A and B). Consistent with increased respiratory rates, energy derivation processes were also significantly enhanced (Supplementary Fig. S12A and B). Conversely, the same analyses in mut-NNS-BS yielded no significant enrichments for DE transcripts and among its proteome; only sugar metabolism was upregulated.

Notably, transcripts and proteins involved in ribonucleotide homeostasis were strongly upregulated in mut-Nab3-BS (Supplementary Fig. S12A and B). Although this biochemical pathway is functionally unrelated to Pic2 in *S. cerevisiae*, several of the enzymes involved are regulated by the NNS complex [54, 59]. To determine if the observed changes in expression of these genes had any impact on nucleotide pools, we performed metabolomic analyses of cell lysates. This revealed a systemic upregulation of metabolites connected to pyrimidine synthesis in mut-Nab3-BS (Supplementary Fig. S12C and D). These findings indicate that the gene expression changes observed in this strain altered its metabolic flux.

Overexpression of human *PIC2* causes energy homeostasis defects

Throughout this work, we focused on *PIC2* partially because mutations in the human Pic2 orthologue, *SLC25A3* [60], are linked to cardiac and muscular diseases [61] and, like *PIC2*, the expression of *SLC25A3* is tightly controlled [62]. Despite not possessing Nrd1 and Nab3 orthologues, mammalian cells employ microRNAs to fine-tune *PIC2* expression [63]. In humans, miR-144 is a key regulator of *SLC25A3* [64]. Similarly to *pic2*D yeast, mammalian cell models lacking *SLC25A3* show mitochondrial hyperpolarization [65] and decreased ATP synthesis [15]. Thus, we investigated whether overexpressing *SLC25A3* would lead to changes in mitochondrial activity resembling that of our *PIC2*-overexpressing yeast model. We used the Flp-In™ system to generate a HEK 293 cell line in which overexpression of *SLC25A3* could be induced with doxycycline (Supplementary Fig. S13). As expected, the mammalian *SLC25A3*-overexpressing model fully recapitulated the mitochondrial hyperpolarization (Fig. 5A) and reduced respiration (Fig. 5B) phenotypes observed in yeast. Additionally, cells overexpressing *SLC25A3* maintained a NADH/NAD$^+$ status similar to that of their uninduced counterparts (Fig. 5C) and showed reduced viability under oxidative challenges (Fig. 5E).

We conclude that suboptimal Pic2 levels in yeast and human cells cause energy homeostasis defects, hindering respiration and causing decreased fitness. Thus, *PIC2* regulation is fundamentally important across species, but organisms have evolved distinct mechanisms to achieve this control. *S. cerevisiae* lacks a microRNA system, so NNS may have evolved to fulfil this regulatory role for *PIC2*. This represents convergent evolution towards the same regulatory outcome using different molecular mechanisms.

It is also important to emphasize that altered expression of *PIC2* did not cause significant changes in yeast or human cell size (Fig. 5H) nor significantly affected yeast cell cycle progression (Fig. 5I and J). Therefore, these results reinforce that the observed cell size abnormalities in mut-Nab3-BS are not directly linked to increased Pic2 protein levels, as *PIC2* overexpression in both yeast and human cells does not impact cell size.

Discussion

Here, we propose a new role for the *S. cerevisiae* NNS complex as a co-transcriptional regulator that ensures homogeneous concentrations of specific proteins across cell populations. Using the copper/phosphate carrier *PIC2* as a model NNS target, we demonstrate that disrupting the binding of Nab3 to yeast *PIC2* causes increased heterogeneity in Pic2 protein concentrations across the population, a redistribution of Nrd1 across its RNA substrates, sequestering of Sen1 on its mRNA, increased *PIC2* mRNA half-life, and aberrant cell size and cell cycle progression. Furthermore, our results suggest that tight control of the protein concentration of this mitochondrial transporter is evolutionarily conserved in both yeast and human cells.

These findings highlight that preventing a single RBP from binding to one low-abundant mRNA target can generate transcriptomic and phenotypic changes that significantly undermine a cell's ability to withstand harsh environments.

The Goldilocks' modulation of PIC2 expression is conserved across eukaryotes

Our results indicate that cells displaying high Pic2 protein levels are penalized when subjected to nutrient restriction or detrimental conditions demanding efficient respiration for survival. We were able to demonstrate this in both yeast and human cells. Interestingly, respiration inhibition and increased susceptibility to extracellular ROS were also observed in mutants lacking *PIC2*. Despite also showing growth defects in our partially respirable raffinose-containing medium, *pic2D* cells are known to perform nearly identically to the parental strain when grown in rich media containing fermentable sugars [14]. These observations align with general microbial adaptive behaviour: while bet hedging enables the development of stochastic phenotypes that may be advantageous for some cells in ideal growth conditions and potentially beneficial for others in future scenarios, adaptation also requires that the expression pattern of some genes becomes "just right". Thus, maintaining *PIC2* expression at a "Goldilocks" level is crucial for optimal cellular function under varying environmental stresses.

Although the expression of *PIC2* and its human homologue (*SLC25A3*) is regulated to control their levels, the regulatory mechanisms involved are markedly different. In human cells, *SLC25A3* regulation involves the microRNA machinery [64], another noise suppression system that is absent in the yeast *S. cerevisiae*. This distinction underscores a fundamental divergence in the molecular strategies evolved by these organisms to achieve gene expression homeostasis.

Previous work suggests that between 10% and 15% of yeast protein-coding genes are regulated by premature transcription termination [34, 66]. It is therefore likely that the NNS complex regulates cellular concentration of other co-regulated protein-coding genes. Similarly to *PIC2*, many of these mRNA targets have been reported to be specifically regulated during adaptation to extracellular challenges: *ADE12* [67], *IMD2* [67–69], *URA2*, and *URA8* are subject to nucleotide availability [59], *FKS2* is responsive to cell wall damage [66], *CLN3* and *MAL33* are controlled during glucose starvation [12, 53], *GPH1* is sensitive to glycogen metabolism [70], as well as *GLT1*, which is dependent on nitrogen metabolism [71]. Furthermore, the exact levels to which this NNS regulatory role occurs are further modulated by the autoregulation of *NRD1*, which is another mRNA target of the NNS complex [52]. Investigating the molecular principle by which NNS tightly controls the concentration of the proteins encoded by its mRNA targets may help to further increase our understanding of mRNA attenuation by polyadenylation site-dependent regulators (e.g. Hrp1 [67], Pcf11 [72], and during DNA repair, Def1 [73, 74], and how these mechanisms interplay to ensure fail-safe termination of protein-coding targets [75–77].

How does a single change in RNA–NNS interactions affect RNA termination across many NNS targets?

We demonstrated that the mut-Nab3-BS strain, which lacks Nab3 binding sites in *PIC2* and expresses the transcript at ∼4-fold higher levels, has altered Nrd1 occupancy on other NNS target transcripts and higher occupancy of Sen1 in *PIC2* mRNAs. We hypothesize that this increased retention time of Sen1 and, possibly, Nrd1 on *PIC2* transcripts can explain the almost doubled half-life of the mut-Nab3-BS *PIC2* mRNA: previous work demonstrated that degradation of NNS target transcripts is required for the recycling of NNS components: previous work from the Libri group showed that degradation of NNS target transcripts is required for the recycling of NNS components [50]. Lack of Nab3 binding therefore likely not only prevents proper termination but also leads to Nrd1/Sen1 sequestration on stabilized *PIC2* transcripts. Such sequestration may also explain the observed redistribution of Nrd1 on ∼4% of known NNS targets. But what was especially striking was that two nucleotide substitutions that block Nab3 binding have such significant impacts on cell size. This implies that the amount of NNS proteins, particularly Sen1, is so limiting that even a relatively small increase in the occupancy of the complex at one of its targets can have significant phenotypic consequences and cause a redistribution of NNS over other targets. The same study from the Libri group showed that overexpression of a degradation-resistant circular RNA decoy can also alter NNS distribution over the transcriptome. Our work shows that a similar effect can be achieved by blocking Nab3 from binding a single low-abundant transcript, demonstrating the exquisite sensitivity of cells to NNS factor availability.

We show that while overexpression of *PIC2* also causes redistribution of NNS components (Supplementary Fig. S10), this does not induce the same cell size and cell division anomalies observed with the mut-Nab3-BS mutant that fails to bind Nab3. Hence, we propose that these cellular phenotypes are a direct result of the sequestration of Sen1 and Nrd1 on *PIC2* in the absence of Nab3. This model implies that Nrd1 and Sen1 can bind RNA independently of Nab3. Indeed, Nrd1 and Nab3 have independent functions [70, 78–82]. Accordingly, previous *in vitro* work has shown that the RRM of Nrd1 can indeed bind RNA independently of Nab3; however, the heterodimer binds RNA with higher affinity [83]. To the best of our knowledge, our analyses provide the first evidence that Nab3-independent recruitment of Nrd1 to an mRNA target of the NNS complex can also occur *in vivo*. It may still be the case, however, that the Nab3–Nrd1 heterodimer still forms on *PIC2* to some extent, but that binding of both proteins to the transcript is required for optimal termination and recycling of the proteins.

Our current working model is that Nab3 binding to *PIC2* is required for efficient recruitment of the exosome complex to the target transcript, which is a plausible explanation for the increased stability of the *PIC2* transcript in the mut-Nab3-BS strain. Alternatively, excess *PIC2* transcripts are translated, and it is possible that Nrd1 and Sen1 could be exported alongside the transcript to the cytoplasm, effectively titrating these proteins away from the nucleus. Indeed, although Nab3, Nrd1, and Sen1 localization is predominantly nuclear, they have all been detected in ribonucleoproteins, which exhibit dynamic cellular localization and could potentially shuttle when bound to their targets [84].

Sequestration of Sen1 and Nrd1 may be occurring through different possible mechanisms. Nab3, which possesses prion-like domains [85], partitions into nuclear granules during nutrient starvation [86]. Despite also containing intrinsically disordered regions, Nrd1 has not been reported to engage in phase separation. Nevertheless, previous work has noted the presence of nucleoids in strains with mutations in the RRM of Nrd1 [53], suggesting that Nrd1 might form condensates in response to environmental stimuli, possibly in conjunction with target transcripts and Nab3. Additionally, Nrd1 and/or Sen1 may be sequestered to different subcellular compartments while still bound to accumulating *PIC2* transcripts in the mut-Nab3-BS mutant.

NNS regulation is integral to achieving optimal cell size and normal cell cycle progression

Our results show that impairing NNS termination of only a single mRNA can cause severe cell size anomalies. Restrictions in Sen1 abundance are known to cause cell cycle [51] and cell division defects [87]. Although no aberrant cell size was assessed in these studies [51, 87], another study provided microscopy evidence suggesting that Sen1-depleted cells become larger [55]. Furthermore, a mere increase in the DNA content resulting from a delayed exit from the G2 phase could theoretically drive a cell size increase [56]. Notably, our mutant was not only oversized but also displayed reduced growth and fitness as well as increased intracellular stress, which coincided with the previous characterization of other oversized models [56]. On this basis, we conclude that our cells are likely exceeding their critical DNA-to-cytoplasm ratio and undergoing cytoplasmic dilution, which was defined as a senescence trait [56]. Consistent with this notion, recent work uncovered that the transcriptome is more heavily regulated by the NNS complex during quiescence [88]. Given that NNS targets are predominantly non-coding, it is possible that these operate as regulators of cell size and, by extension, affect the cell cycle. However, the function of many ncRNAs in yeast remains uncharacterized.

Our work reinforces the notion that NNS-mediated attenuation of mRNAs acts as a mechanism to coordinate the expression of functionally related protein-coding genes, possibly involved in cell cycle regulation, in response to environmental cues. Our results imply that the levels of such targets would be subject to changes in NNS availability. In this respect, NNS would behave like a class-specific transcription factor to fine-tune the expression of target genes.

Our results also outline a principle by which global transcriptional alterations can originate in any type of cell. By creating an imbalance in the binding stoichiometry of the RNA-recognition proteins of a transcription termination complex in one single transcript, it is possible to constrain the recycling of the components of such a complex and, ultimately, disturb the homeostasis of other target species. In turn, the resulting gene expression pattern can drive phenotypic defects that reduce cell fitness and elicit cellular defects.

Acknowledgements

We would like to thank Domenico Libri, Mordechai (Motti) Choder, Ramon Grima and Julien Hurbain for critically reading the manuscript and providing valuable feedback. We would like to thank Ivan Clark, Alán Muñoz González, Lori Koch, Tessa Moses, Roopesh Krishnankutty, Martin Waterfall, David Kelly, Toni McHugh, and Sam Ranasinghe for their valuable discussions, helpful advice, and technical assistance.

The metabolomics analyses were carried out by the EdinOmics research facility (RRID: SCR_021838) at the University of Edinburgh. MS/MS was performed at the Mass Spectrometry Facility of the Institute of Genetics and Cancer (IGC) of the University of Edinburgh. Flow cytometry data were generated within the Flow Cytometry and Cell Sorting Facility in the Ashworth Building at the University of Edinburgh. The facility is supported by funding from the Wellcome Trust and the University of Edinburgh. Training for confocal imaging was performed in the Centre Optical Instrumentation Laboratory (COIL), which is supported by a Core Grant (203149) to the Wellcome Centre for Cell Biology at the University of Edinburgh, and images were acquired at the Medical Sciences Confocal Imaging Facility at University College London. The Flp-In™ kit and the BY4742 strain were gifts from David Tollervey and Adele Marston, respectively.

Author contributions: Conceptualization: S.G., P.S.S., M.D., and S.E-S. Methodology: S.G., P.S.S., M.D., and S.E-S. Investigation: S.E-S., T.W., M.G., I.F., P.S.S., and S.G. Visualization: S.E-S., P.S.S., and S.G. Writing—original draft: S.E-S. and S.G. Writing—review and editing: all authors. Supervision and funding acquisition: S.E-S., M.D., P.S.S., and S.G.

Supplementary data

Supplementary data is available at NAR online.

Conflict of interest

The authors declare that they have no conflicts of interest.

Funding

This work was supported by a Medical Research Council Non-Clinical Senior Research Fellowship (MR/R008205/1) to S.G., a Wellcome Trust PhD training fellowship (224 084/Z/21/Z) and a Microbiology Society Research Visit Grant (GA003916) awarded to S.E-S., a Leverhulme Trust Grant (RPG-2018-004) and a Biotechnology and Biological Sciences Research Council Grant (BB/R001359/1) to P.S.S., and a Erasmus + traineeship to T.W. Funding to pay the Open Access publication charges for this article was provided by UKRI open access funds.

Data availability

The raw mass spectrometry proteomic data and accompanying files have been deposited at the ProteomeXchange Consortium via the PRIDE[58] partner repository. The accession number is PXD055087. The raw and processed RNA-sequencing data have been deposited in the NCBI Gene Expression Omnibus (GEO) under accession number GSE276521. Raw and processed data for the CRAC libraries derived from Nab3, Nrd1, Sen1, and RNA polymerase (Rpo21) have also been uploaded to NCBI GEO under accession numbers GSE276517, GSE276519, GSE276524, GSE305097, and GSE305098. The code for analysing differential binding of RNA-binding proteins is available from Zenodo (https://doi.org/10.5281/zenodo.16811404) and the Granneman lab repository (https://git.ecdf.ed.ac.uk/sgrannem/dbpeaks/-/releases/testdata).

References

1. Marguerat S, Lawler K, Brazma A *et al.* Contributions of transcription and mRNA decay to gene expression dynamics of fission yeast in response to oxidative stress. *RNA Biol* 2014;11:702–14. https://doi.org/10.4161/rna.29196
2. Kriner MA, Sevostyanova A, Groisman EA. Learning from the leaders: gene regulation by the transcription termination factor Rho. *Trends Biochem Sci* 2016;41:690–9. https://doi.org/10.1016/j.tibs.2016.05.012
3. Porrua O, Libri D. Transcription termination and the control of the transcriptome. *Nat Rev Mol Cell Biol* 2015;16:190–202. https://doi.org/10.1038/nrm3943
4. Steinmetz EJ, Conrad NK, Brow DA *et al.* RNA-binding protein Nrd1 directs poly(A)-independent 3′-end formation of RNA polymerase II transcripts. *Nature* 2001;413:327–31. https://doi.org/10.1038/35095090
5. Thiebaut M, Kisseleva-Romanova E, Rougemaille M *et al.* Transcription termination and nuclear degradation of cryptic unstable transcripts: a role for the Nrd1–Nab3 pathway in genome surveillance. *Mol Cell* 2006;23:853–64. https://doi.org/10.1016/j.molcel.2006.07.029
6. Schulz D, Schwalb B, Kiesel A *et al.* Transcriptome surveillance by selective termination of noncoding RNA synthesis. *Cell* 2013;155:1075. https://doi.org/10.1016/j.cell.2013.10.024
7. Porrua O, Libri D. A bacterial-like mechanism for transcription termination by the Sen1p helicase in budding yeast. *Nat Struct Mol Biol* 2013;20:884–91. https://doi.org/10.1038/nsmb.2592
8. Skourti-Stathaki K, Proudfoot NJ, Gromak N. Human senataxin resolves RNA/DNA hybrids formed at transcriptional pause sites to promote Xrn2-dependent termination. *Mol Cell* 2011;42:794–805. https://doi.org/10.1016/j.molcel.2011.04.026
9. Estell C, West S. ZC3H4/restrictor exerts a stranglehold on pervasive transcription. *J Mol Biol* 2025;437:168707. https://doi.org/10.1016/j.jmb.2024.168707
10. Vasiljeva L, Kim M, Mutschler H *et al.* The Nrd1–Nab3–Sen1 termination complex interacts with the Ser5-phosphorylated RNA polymerase II C-terminal domain. *Nat Struct Mol Biol* 2008;15:795–804. https://doi.org/10.1038/nsmb.1468
11. Bresson S, Tuck A, Staneva D *et al.* Nuclear RNA decay pathways aid rapid remodeling of gene expression in yeast. *Mol Cell* 2017;65:787–800.e5. https://doi.org/10.1016/j.molcel.2017.01.005
12. van Nues R, Schweikert G, de Leau E *et al.* Kinetic CRAC uncovers a role for Nab3 in determining gene expression profiles during stress. *Nat Commun* 2017;8:12. https://doi.org/10.1038/s41467-017-00025-5
13. Hamel P, Saint-Georges Y, De Pinto B *et al.* Redundancy in the function of mitochondrial phosphate transport in Saccharomyces cerevisiae and *Arabidopsis thaliana*. *Mol Microbiol* 2004;51:307–17. https://doi.org/10.1046/j.1365-2958.2003.03810.x
14. Vest KE, Leary SC, Winge DR *et al.* Copper import into the mitochondrial matrix in *Saccharomyces cerevisiae* is mediated by Pic2, a mitochondrial carrier family protein. *J Biol Chem* 2013;288:23884–92. https://doi.org/10.1074/jbc.M113.470674
15. Peoples JN, Ghazal N, Duong DM *et al.* Loss of the mitochondrial phosphate carrier SLC25A3 induces remodeling of the cardiac mitochondrial protein acylome. *Am J Physiol-Cell Physiol* 2021;321:C519–34. https://doi.org/10.1152/ajpcell.00156.2021
16. Oehler VG, Ka YY, Choi YE *et al.* The derivation of diagnostic markers of chronic myeloid leukemia progression from microarray data. *Blood* 2009;114:3292–8. https://doi.org/10.1182/blood-2009-03-212969
17. Brachmann CB, Davies A, Cost GJ *et al.* Designer deletion strains derived from *Saccharomyces cerevisiae* S288C : a useful set of strains and plasmids for PCR-mediated gene disruption and other applications. *Yeast* 1998;132:115–32.
18. Longtine MS, McKenzie A, Demarini DJ *et al.* Additional modules for versatile and economical PCR-based gene deletion and modification in *Saccharomyces cerevisiae*. *Yeast* 1998;14:953–61. https://doi.org/10.1002/(SICI)1097-0061(199807)14:10⟨953::AID-YEA293⟩3.0.CO;2-U
19. Janke C, Magiera MM, Rathfelder N *et al.* A versatile toolbox for PCR-based tagging of yeast genes: new fluorescent proteins, more markers and promoter substitution cassettes. *Yeast* 2004;21:947–62. https://doi.org/10.1002/yea.1142
20. Granneman S, Kudla G, Petfalski E *et al.* Identification of protein binding sites on U3 snoRNA and pre-rRNA by UV cross-linking and high-throughput analysis of cDNAs. *Proc Natl Acad Sci USA* 2009;106:9613 LP–9618. https://doi.org/10.1073/pnas.0901997106
21. Bähler J, Wu JQ, Longtine MS *et al.* Heterologous modules for efficient and versatile PCR-based gene targeting in *Schizosaccharomyces pombe*. *Yeast* 1998;14:943–51. https://doi.org/10.1002/(SICI)1097-0061(199807)14:10⟨943::AID-YEA292⟩3.0.CO;2-Y
22. Borek WE, Vincenten N, Duro E *et al.* The proteomic landscape of centromeric chromatin reveals an essential role for the Ctf19CCAN complex in meiotic kinetochore assembly. *Curr Biol* 2021;31:283–296.e7. https://doi.org/10.1016/j.cub.2020.10.025
23. Williams TC, Espinosa MI, Nielsen LK *et al.* Dynamic regulation of gene expression using sucrose responsive promoters and RNA interference in *Saccharomyces cerevisiae*. *Microb Cell Fact* 2015;14:1–10. https://doi.org/10.1186/s12934-015-0223-7
24. Sikorski RS, Hieter P. A system of shuttle vectors and yeast host strains designed for efficient manipulation of DNA in Saccharomyces cerevisiae. *Genetics* 1989;122:19–27. https://doi.org/10.1093/genetics/122.1.19
25. Montaño-Gutierrez LF, Correia K, Swain PS. Multiple nutrient transporters enable cells to mitigate a rate-affinity tradeoff. *PLoS Comput Biol* 2022;18:1–16.
26. Trcek T, Larson DR, Moldón A *et al.* Single-molecule mRNA decay measurements reveal promoter-regulated mRNA stability in yeast. *Cell* 2011;147:1484–97. https://doi.org/10.1016/j.cell.2011.11.051
27. McKellar SW, Ivanova I, van Nues RW *et al.* Monitoring protein–RNA interaction dynamics *in vivo* at high temporal resolution using χCRAC. *J Visualized Exp* 2020. https://dx.doi.org/10.3791/61027.
28. Chu LC, Arede P, Li W *et al.* The RNA-bound proteome of MRSA reveals post-transcriptional roles for helix-turn-helix DNA-binding and Rossmann-fold proteins. *Nat Commun* 2022;13:2883.

29. Gancedo JM, Gancedo C. Concentrations of intermediary metabolites in yeast. *Biochimie* 1973;55:205–11. https://doi.org/10.1016/S0300-9084(73)80393-1
30. Pollak N, Dölle C, Ziegler M. The power to reduce: pyridine nucleotides–small molecules with a multitude of functions. *Biochem J* 2007;402:205–18. https://doi.org/10.1042/BJ20061638
31. Duchen MR, Surin A, Jacobson J. Imaging mitochondrial function in intact cells. *Methods Enzymol* 2003;361:353–89.
32. Pičmanová M, Moses T, Cortada J *et al.* Rapid HILIC Z ion mobility mass spectrometry (RHIMMS) method for untargeted metabolomics of complex biological samples. *Metabolomics* 2022;18:16.
33. Pang Z, Chong J, Zhou G *et al.* 2021; MetaboAnalyst 5. 0 : narrowing the gap between raw spectra and functional insights. *Nucleic Acids Res* 49:388–96.
34. Webb S, Hector RD, Kudla G *et al.* PAR-CLIP data indicate that Nrd1-Nab3-dependent transcription termination regulates expression of hundreds of protein coding genes in yeast. *Genome Biol* 2014;15:R8. https://doi.org/10.1186/gb-2014-15-1-r8
35. Dodt M, Roehr JT, Ahmed R *et al.* FLEXBAR—flexible barcode and adapter processing for next-generation sequencing platforms. *Biology (Basel)* 2012;1:895–905.
36. Quinlan AR, Hall IM. BEDTools: a flexible suite of utilities for comparing genomic features. *Bioinformatics* 2010;26:841–2. https://doi.org/10.1093/bioinformatics/btq033
37. Love MI, Huber W, Anders S. Moderated estimation of fold change and dispersion for RNA-seq data with DESeq2. *Genome Biol* 2014;15:550. https://doi.org/10.1186/s13059-014-0550-8
38. Cordiner RA, Dou Y, Thomsen R *et al.* Temporal-iCLIP captures co-transcriptional RNA-protein interactions. *Nat Commun* 2023;14:696.
39. Allan C, Burel J-M, Moore J *et al.* OMERO: flexible, model-driven data management for experimental biology. *Nat Meth* 2012;9:245–53.
40. Muñoz González AF, Wongprommoon A, Swain PS. 2024; ALIBY (Analyser of Live-cell Imaging for Budding Yeast) GitLab repository. https://gitlab.com/aliby/aliby, accessed 3 May 2024.
41. Pietsch JMJ, Muñoz AF, Adjavon DYA *et al.* Determining growth rates from bright-field images of budding cells through identifying overlaps. *eLife* 2023;12 https://doi.org/10.7554/eLife.79812
42. Montaño-Gutierrez LF, Moreno NM, Farquhar IL *et al.* Analysing and meta-analysing time-series data of microbial growth and gene expression from plate readers. *PLoS Comput Biol* 2022;18:e1010138. https://doi.org/10.1371/journal.pcbi.1010138
43. Schneider CA, Rasband WS, Eliceiri KW. NIH Image to ImageJ: 25 years of image analysis. *Nat Methods* 2012;9:671–5.
44. Cox J, Mann M. MaxQuant enables high peptide identification rates, individualized p.p.b.-range mass accuracies and proteome-wide protein quantification. *Nat Biotechnol* 2008;26:1367–72. https://doi.org/10.1038/nbt.1511
45. Cox J, Neuhauser N, Michalski A *et al.* Andromeda: a peptide search engine integrated into the MaxQuant environment. *J Proteome Res* 2011;10:1794–805. https://doi.org/10.1021/pr101065j
46. Tyanova S, Temu T, Sinitcyn P *et al.* The Perseus computational platform for comprehensive analysis of (prote)omics data. *Nat Methods* 2016;13:731–40. https://doi.org/10.1038/nmeth.3901
47. Robinson MD, McCarthy DJ, Smyth GK. edgeR: a Bioconductor package for differential expression analysis of digital gene expression data. *Bioinformatics* 2009;26:139–40. https://doi.org/10.1093/bioinformatics/btp616
48. Thomas PD, Ebert D, Muruganujan A *et al.* PANTHER: making genome-scale phylogenetics accessible to all. *Protein Sci* 2022;31:8–22. https://doi.org/10.1002/pro.4218
49. Dale RK, Pedersen BS, Quinlan AR. Pybedtools: a flexible Python library for manipulating genomic datasets and annotations. *Bioinformatics* 2011;27:3423–4. https://doi.org/10.1093/bioinformatics/btr539
50. Villa T, Barucco M, Martin-Niclos M-J *et al.* Degradation of non-coding RNAs promotes recycling of termination factors at sites of transcription. *Cell Rep* 2020;32:107942. https://doi.org/10.1016/j.celrep.2020.107942
51. Mischo HE, Chun Y, Harlen KM *et al.* Cell-cycle modulation of transcription termination factor Sen1. *Mol Cell* 2018;70:312–26. https://doi.org/10.1016/j.molcel.2018.03.010
52. Arigo JT, Eyler DE, Carroll KL *et al.* Termination of cryptic unstable transcripts is directed by yeast RNA-binding proteins Nrd1 and Nab3. *Mol Cell* 2006;23:841–51. https://doi.org/10.1016/j.molcel.2006.07.024
53. Darby MM, Serebreni L, Pan X *et al.* The *Saccharomyces cerevisiae* Nrd1–Nab3 transcription termination pathway acts in opposition to Ras signaling and mediates response to nutrient depletion. *Mol Cell Biol* 2012;32:1762–75. https://doi.org/10.1128/MCB.00050-12
54. Ajazi A, Choudhary R, Tronci L *et al.* CTP sensing and Mec1 ATR-Rad53 CHK1/CHK2 mediate a two-layered response to inhibition of glutamine metabolism. *PLoS Genet* 2022;18:e1010101. https://doi.org/10.1371/journal.pgen.1010101
55. Aiello U, Challal D, Wentzinger G *et al.* Sen1 is a key regulator of transcription-driven conflicts. *Mol Cell* 2022;82:2952–66. https://doi.org/10.1016/j.molcel.2022.06.021
56. Neurohr GE, Terry RL, Lengefeld J *et al.* Excessive cell growth causes cytoplasm dilution and contributes to senescence. *Cell* 2019;176:1083–97. https://doi.org/10.1016/j.cell.2019.01.018
57. Haruki H, Nishikawa J, Laemmli UK. The anchor-away technique: rapid, conditional establishment of yeast mutant phenotypes. *Mol Cell* 2008;31:925–32. https://doi.org/10.1016/j.molcel.2008.07.020
58. Barbet NC, Schneider U, Helliwell SB *et al.* TOR controls translation initiation and early G1 progression in yeast. *MBoC* 1996;7:25–42. https://doi.org/10.1091/mbc.7.1.25
59. Thiebaut M, Colin J, Neil H *et al.* Futile cycle of transcription initiation and termination modulates the response to nucleotide shortage in *S. cerevisiae*. *Mol Cell* 2008;31:671–82. https://doi.org/10.1016/j.molcel.2008.08.010
60. Boulet A, Vest KE, Maynard MK *et al.* The mammalian phosphate carrier SLC25A3 is a mitochondrial copper transporter required for cytochrome c oxidase biogenesis. *J Biol Chem* 2018;293:1887–96. https://doi.org/10.1074/jbc.RA117.000265
61. Mayr JA, Merkel O, Kohlwein SD *et al.* Mitochondrial phosphate-carrier deficiency: a novel disorder of oxidative phosphorylation. *Am J Human Genet* 2007;80:478–84. https://doi.org/10.1086/511788
62. Padovan-Merhar O, Nair GP, Biaesch AG *et al.* Single mammalian cells compensate for differences in cellular volume and DNA copy number through independent global transcriptional mechanisms. *Mol Cell* 2015;58:339–52. https://doi.org/10.1016/j.molcel.2015.03.005
63. Siciliano V, Garzilli I, Fracassi C *et al.* MiRNAs confer phenotypic robustness to gene networks by suppressing biological noise. *Nat Commun* 2013;4:2364. https://doi.org/10.1038/ncomms3364
64. Baseler WA, Thapa D, Jagannathan R *et al.* miR-141 as a regulator of the mitochondrial phosphate carrier (Slc25a3) in the type 1 diabetic heart. *Am J Physiol-Cell Physiol* 2012;303:C1244–51. https://doi.org/10.1152/ajpcell.00137.2012
65. Wolf SG, Mutsafi Y, Dadosh T *et al.* 3D visualization of mitochondrial solid-phase calcium stores in whole cells. *eLife* 2017;6:e29929. https://doi.org/10.7554/eLife.29929
66. Kim KY, Levin DE. Mpk1 MAPK association with the paf1 complex blocks sen1-mediated premature transcription termination. *Cell* 2011;144:745–56. https://doi.org/10.1016/j.cell.2011.01.034
67. Kuehner JN, Brow DA. Regulation of a eukaryotic gene by GTP-dependent start site selection and transcription attenuation. *Mol Cell* 2008;31:201–11. https://doi.org/10.1016/j.molcel.2008.05.018

68. Steinmetz EJ, Warren CL, Kuehner JN *et al.* Genome-wide distribution of yeast RNA polymerase II and its control by Sen1 helicase. *Mol Cell* 2006;24:735–46. https://doi.org/10.1016/j.molcel.2006.10.023
69. Jenks MH, O'Rourke TW, Reines D. Properties of an intergenic terminator and start site switch that regulate IMD2 transcription in yeast. *Mol Cell Biol* 2008;28:3883–93. https://doi.org/10.1128/MCB.00380-08
70. Chen X, Poorey K, Carver MN *et al.* Transcriptomes of six mutants in the Sen1 pathway reveal combinatorial control of transcription termination across the *Saccharomyces cerevisiae* genome. *PLoS Genet* 2017;13:e1006863. https://doi.org/10.1371/journal.pgen.1006863
71. Merran J, Corden JL. Yeast RNA-binding protein Nab3 regulates genes involved in nitrogen metabolism. *Mol Cell Biol* 2017;37:154–71. https://doi.org/10.1128/MCB.00154-17
72. Creamer TJ, Darby MM, Jamonnak N *et al.* Transcriptome-wide binding sites for components of the *Saccharomyces cerevisiae* non-poly(A) termination pathway: nrd1, Nab3, and Sen1. *PLoS Genet* 2011;7:e1002329. https://doi.org/10.1371/journal.pgen.1002329.
73. Whalen C, Tuohy C, Tallo T *et al.* RNA polymerase II transcription attenuation at the yeast DNA repair gene, DEF1, involves Sen1-dependent and polyadenylation site-dependent termination. *G3 (Bethesda)* 2018;8:2043–58. https://doi.org/10.1534/g3.118.200072
74. Amodeo ME, Mitchell SPC, Pavan V *et al.* RNA polymerase II transcription attenuation at the yeast DNA repair gene DEF1 is biologically significant and dependent on the Hrp1 RNA-recognition motif. *G3 (Bethesda)* 2023;13:jkac292. https://doi.org/10.1093/g3journal/jkac292
75. Grzechnik P, Gdula MR, Proudfoot NJ. Pcf11 orchestrates transcription termination pathways in yeast. *Genes Dev* 2015;29:849. https://doi.org/10.1101/gad.251470.114
76. Graber JH, Hoskinson D, Liu H *et al.* Mutations in yeast Pcf11, a conserved protein essential for mRNA 3′ end processing and transcription termination, elicit the environmental stress response. *Genetics* 2024;226:iyad199. https://doi.org/10.1093/genetics/iyad199
77. Kuehner JN, Pearson EL, Moore C. Unravelling the means to an end: RNA polymerase II transcription termination. *Nat Rev Mol Cell Biol* 2011;12:283–94. https://doi.org/10.1038/nrm3098
78. Fasken MB, Laribee RN, Corbett AH. Nab3 facilitates the function of the TRAMP complex in RNA processing via recruitment of Rrp6 independent of Nrd1. *PLoS Genet* 2015;11:e1005044. https://doi.org/10.1371/journal.pgen.1005044
79. Honorine R, Mosrin-Huaman C, Hervouet-Coste N *et al.* Nuclear mRNA quality control in yeast is mediated by Nrd1 co-transcriptional recruitment, as revealed by the targeting of Rho-induced aberrant transcripts. *Nucleic Acids Res* 2011;39:2809–20. https://doi.org/10.1093/nar/gkq1192
80. Han Z, Jasnovidova O, Haidara N *et al.* Termination of non-coding transcription in yeast relies on both an RNA Pol II CTD interaction domain and a CTD-mimicking region in Sen1. *EMBO J* 2020;39:e101548. https://doi.org/10.15252/embj.2019101548
81. Singh P, Chaudhuri A, Banerjea M *et al.* Nrd1p identifies aberrant and natural exosomal target messages during the nuclear mRNA surveillance in Saccharomyces cerevisiae. *Nucleic Acids Res* 2021;49:11512–36. https://doi.org/10.1093/nar/gkab930
82. Chaves-Arquero B, Martínez-Lumbreras S, Camero S *et al.* Structural basis of Nrd1–Nab3 heterodimerization. *Life Sci Alliance* 2022;5:e202101252, https://doi.org/10.26508/lsa.202101252.
83. Carroll KL, Ghirlando R, Ames JM *et al.* Interaction of yeast RNA-binding proteins Nrd1 and Nab3 with RNA polymerase II terminator elements. *RNA* 2007;13:361–73, https://doi.org/10.1261/rna.338407.
84. Mitchell SF, Jain S, She M *et al.* Global analysis of yeast mRNPs. *Nat Struct Mol Biol* 2013;20:127–33. https://doi.org/10.1038/nsmb.2468
85. O'Rourke TW, Reines D. Determinants of amyloid formation for the yeast termination factor nab3. *PLoS One* 2016;11:e0150865.
86. Loya TJ, O'Rourke TW, Simke WC *et al.* Nab3's localization to a nuclear granule in response to nutrient deprivation is determined by its essential prion-like domain. *PLoS One* 2018;13:e0209195. https://doi.org/10.1371/journal.pone.0209195
87. Choudhary R, Niska-Blakie J, Adhil M *et al.* Sen1 and Rrm3 ensure permissive topological conditions for replication termination. *Cell Rep* 2023;42:112747. https://doi.org/10.1016/j.celrep.2023.112747
88. Greenlaw AC, Alavattam KG, Tsukiyama T. Post-transcriptional regulation shapes the transcriptome of quiescent budding yeast. *Nucleic Acids Res* 2023;52:1043–63. https://doi.org/10.1093/nar/gkad1147

Received: February 4, 2025. **Revised:** October 8, 2025. **Accepted:** October 9, 2025